

Fast finite element modelling of bridled leading-edge inflatable kites

P.I.H. Roeleveld



Fast finite element modelling of bridled leading-edge inflatable kites

by

P.I.H. Roeleveld

Responsible Supervisor: Dr.-Ing. R. Schmehl
Daily Supervisor: Ir. J. Poland
Institution: Delft University of Technology
Place: Faculty of Aerospace Engineering, Delft
Date Friday 14th November, 2025

Cover: TU Delft V3 kite



Contents

Nomenclature	v
Preface	vii
Summary	viii
1 Introduction	1
1.1 Airborne Wind Energy	1
1.2 V3 Kite	1
1.3 Motivation	2
2 Literature Review	4
2.1 Aero-structural coupling	4
2.2 Deformations	6
2.3 Vibrations	6
2.4 Structural Models	8
2.4.1 Models without deformation	8
2.4.2 Multi-plate	8
2.4.3 Lumped mass / Particle System	8
2.4.4 Multi-body	9
2.4.5 Finite Element	9
2.5 Non-Linear Modelling	9
2.5.1 Geometric non-linearity	9
2.5.2 Form Finding	11
2.6 Beam Modelling	12
2.6.1 Inflatable Beams	12
2.6.2 Beam Modelling in FEM	13
2.6.3 Beam Modelling in PSM	14
2.7 Research objective and questions	15
3 Modelling Approach	16
3.1 Aero-structural model	16
3.2 Structural model	17
3.3 Aerodynamic model	18
4 Finite element framework for kites	19
4.1 Finite element formulation	19
4.2 Kite-specific elements	22
4.2.1 Bridle line system	22
4.2.2 Leading edge and struts	23
4.2.3 Canopy	26
4.3 Newton-Raphson iteration	26
4.4 Verification	27
4.4.1 Saddle problem	27
4.4.2 Nested pulleys	28

4.4.3 Inflatable beam	29
5 V3 Kite Model	30
5.1 Simplified Model	30
5.2 Complete Model	30
5.3 Model validation	30
5.4 Aero-structural coupling	30
6 Results	34
7 Conclusion	35
8 Discussion	36
References	37

List of Figures

1.1	TU Delft V3 Kite overview showing the kite and bridle configuration, adapted from [9, 31]	2
1.2	(a) TU Delft V3 Kite and bridle lines, the red bridle lines are simplified in a PSM. (b) The PSM of the V3 kite with a simplified bridle system.	3
2.1	Partitioned and Monolithic FSI methods [27]	5
2.2	FSI model of the TU Delft V3 Kite [35]	5
2.3	Kite deformation due to inputs from the kite control unit [34]. (a) Asymmetric deformation (red) due to a steering input on the kite from the powered state (grey). (b) Depowering of the kite (red) from the powered state (grey)	6
2.4	Kite deformation modes experienced during a pumping-cycle operation [27]	7
2.5	Variation in DOF of developed LEI structural model types, model figures from [4, 6, 19]	8
2.6	Example of geometric non-linear behaviour [4]. (a) Forces in a non-deflected situation. (b) Forces in a deflected situation. (c) Linear deflection. (d) Non-linear deflection	11
2.7	Development of various form-finding methods and their respective references, with arrows denoting descendants, dotted lines denoting related but independent methods and triangles denoting a first formulation of surface elements [43]	12
2.8	Stress-strain curve of a homogenous isotropic beam and an inflated tubular beam [2, 5]	13
2.9	Beam representation in a PSM based on rigid pyramids hinged with rotational springs [21].	14
2.10	Equivalent beam segment and particle spring assembly used to represent a beam in PSM [47, 45]	14
3.1	Schematic overview of the partitioned aero-structural model	16
3.2	Schematic overview of the finite element model	17
3.3	Schematic overview of the vortex step method	18
4.1	A two node element in three-dimensional space with six DOF per node, accompanied by a local coordinate system [4] TODO: replace by own figure	19
4.2	Coordinate system rotations around the x,y and z axes.	20
4.3	Internal forces of a line between n_1 and n_2	23
4.4	Internal forces of a pulley between n_1 , n_2 and n_3 , where n_2 is the pulley node	23
4.5	(a) Quadrilateral representation of part of a canopy. (b) Example of canopy discretisation within a kite segment	26
4.6	(a) Initial conditions of a 5×5 saddle form problem (b) Converged solution of 5×5 saddle form problem.	27
4.7	(a) Initial conditions of a nested pulley system (b) Converged solution of the nested pulley system.	28

4.8	Comparison of 1 meter beam elements with Breukel's equations for inflatable beams, scatter points indicate results from the FEM, lines indicate breukel's equations	29
5.1	Caption (maybe put in appendix)	31
5.2	V3.25 Kite bridle configuration (maybe put in appendix)	32
5.3	Modified V3.25 Kite bridle configuration for gravity test (maybe put in appendix)	33

List of Tables

2.1	An overview of structural models for modelling a LEI kite in order of increasing DOFs.	10
4.1	Comparison between FEM and PSM for various saddle problem sizes.	28
4.2	Pulley line angles from converged state of the nested pulley system	28

Nomenclature

Abbreviations

Abbreviation	Definition
AWE	Airborne wind energy
CAD	Computer aided design
CFD	Computational fluid dynamics
DOF	Degrees of freedom
FEM	Finite element model
FSI	Fluid-structure interaction
LEI	Leading edge inflatable
PSM	Particle System model
VSM	Vortex step method

Symbols

Symbol	Definition	Unit
C	Damping Matrix	kg s^{-1}
E	Young's modulus	Pa
F_{tip}	Applied tip load	N
I	Area moment of inertia	m^4
K	Stiffness matrix	N m^{-1}
K_e	Elastic stiffness matrix	N m^{-1}
K_g	Geometric stiffness matrix	N m^{-1}
l	Length	m
M	Mass matrix	kg
P	Force vector	N
p	Pressure	Pa
r	Radius	m
T	Torque	N m
v	Deflection	m
x	Displacement vector	m
\dot{x}	Velocity vector	m s^{-1}
\ddot{x}	Acceleration vector	m s^{-2}
ϕ	Torsion angle	rad

Preface

A preface...

*P.I.H. Roeleveld
Delft, November 2025*

Summary

A summary...

1

Introduction

1.1. Airborne Wind Energy

The airborne wind energy sector seeks to make wind energy available at a lower material cost by harvesting wind energy using kites. A large part of the sector is dedicated to producing wind power with pumping cycles using soft-wing kites. A pumping cycle consists of a reel-out, generating energy, and a reel-in phase, consuming energy. Flying the kite crosswind during reel-out and depowering the kite during reel-in leads to a net energy gain over the pumping cycle. With the upscaling of kites from 10 m^2 to surface areas up to 500 m^2 , reliance on computational methods for kites has increased. Conventional kite design methods rely on experimental testing, but this method has become too expensive, time-consuming, and risky for AWE applications.

1.2. V3 Kite

At the Delft University of Technology, research and development of AWE systems has led to various kites and the spin-off company Kitepower. The developed kites are soft-wing leading-edge inflatable (LEI) kites similar to those used in kitesurfing applications. The LEI Kite uses an inflatable beam along the leading edge and several smaller beams, called struts, along the wing's chord to define the structure's shape. The TU Delft V3 kite, as seen in Figure 1.1, has been used extensively in literature. Its data is open-source available, including computer-aided design (CAD) files, computational fluid dynamics (CFD) analysis, flight tests, and much more [33].

Modelling a kite's dynamics, aerodynamics, and deformation through simulation is difficult, as the problem is non-linear. Bosch [4] notes three sources of non-linearities in a LEI kite. Geometric non-linearities, material non-linearities, and force non-linearities are all apparent in a LEI kite and must be accounted for in a model. A detailed explanation of the three non-linearities is given.

- **Geometric non-linearity:** A kite undergoes large displacements and rotations leading to significant changes in its geometry during flight. A linear approach to structural modelling is no longer accurate in such cases, as it assumes small deformations and constant stiffness. The model needs to account for the change in structural stiffness and internal force distribution due to the change in geometry.
- **Material non-linearity:** Material non-linearities are apparent in the inflatable structures in the kite. The Young's modulus depends on the beam's deflection [6]. Material non-

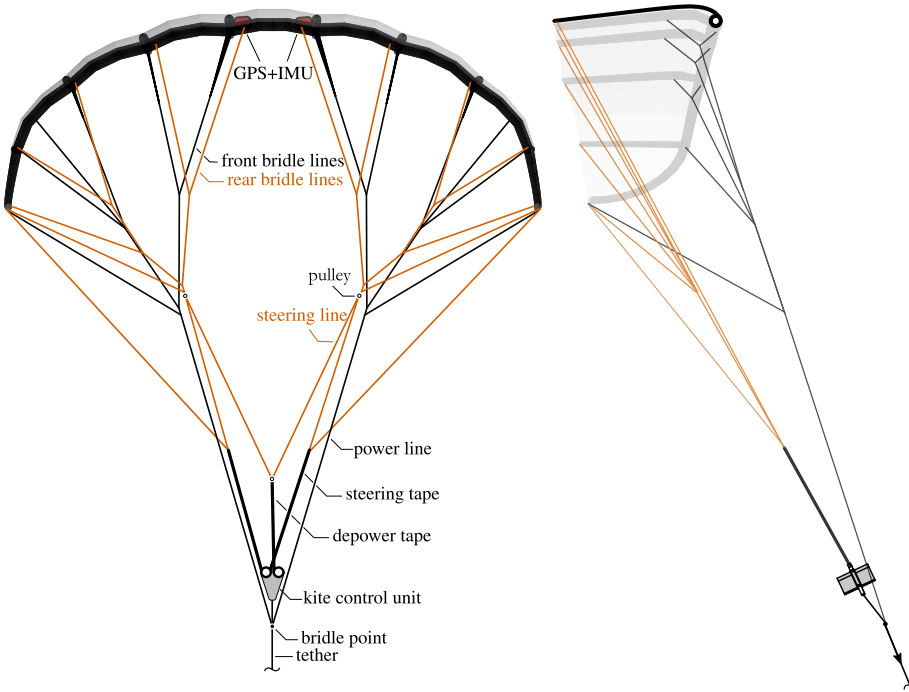


Figure 1.1: TU Delft V3 Kite overview showing the kite and bridle configuration, adapted from [9, 31]

linearities are also evident in the membrane material, which is a woven material and a complex structure exhibiting non-linear stress-strain behaviour [41].

- **Force non-linearity:** A kite's aerodynamic load depends on its shape, which changes as the kite deforms. The external forces are not fixed and change as the structure deforms, leading to a force non-linearity. As a result, the problem becomes a fluid-structure interaction (FSI) problem, where the aerodynamics and deformation influence each other.

This thesis aims to develop a structural model to use inside an FSI solver for a leading-edge inflatable kite. The structural model will resolve the bending properties of the inflatable structures inside the kite.

1.3. Motivation

Structural models of kites reported in the literature that capture deformation often rely on commercial software, require calibration of parameters, or lack robustness[4, 6]. Poland and Schmehl [34] developed a structural model specifically for aero-structural coupled problems. The model is based on lumped mass particles connected by spring-damper elements. Such a particle system model (PSM) is well-suited as a structural model for a soft-wing kite because it can resolve the bridle line system, which dominates the shape of a soft-wing kite [34]. The model enforces the canopy into quadrilateral sections where each corner is connected to the others with a spring.

One limitation of the PSM lies in its treatment of the bridle line system. In the physical V3 kite, the bridle lines attach at multiple points along the wing chord. The spring-damper elements can transmit tensile and compressive forces, but lack rotational resistance at the connection points. Therefore, the bridle lines can only be introduced at the strut's endpoints. Attempting to represent additional attachment points by introducing multiple spring-damper elements along the chord produces a non-physical response. To address this, the bridle line system was

adapted. Fig. 1.2(a) shows the physical V3 kite, whereas Fig. 1.2(b) shows the adapted kite for the PSM. This simplification can be resolved by including the bending stiffness of the leading edge and struts. However, including bending stiffness in a PSM can come at a significant computational cost [21].

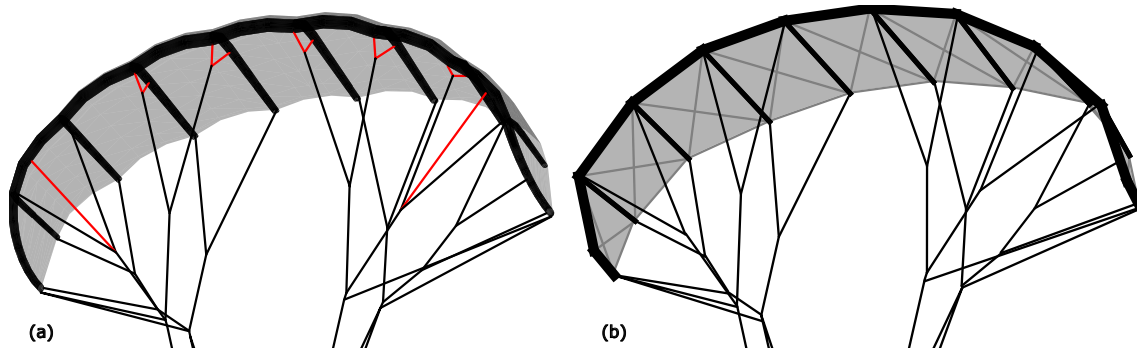


Figure 1.2: (a) TU Delft V3 Kite and bridle lines, the red bridle lines are simplified in a PSM. (b) The PSM of the V3 kite with a simplified bridle system.

2

Literature Review

TODO: kite terminology should be in the literature TODO: Clean up unnecessary information
TODO: introduce aerodynamic model

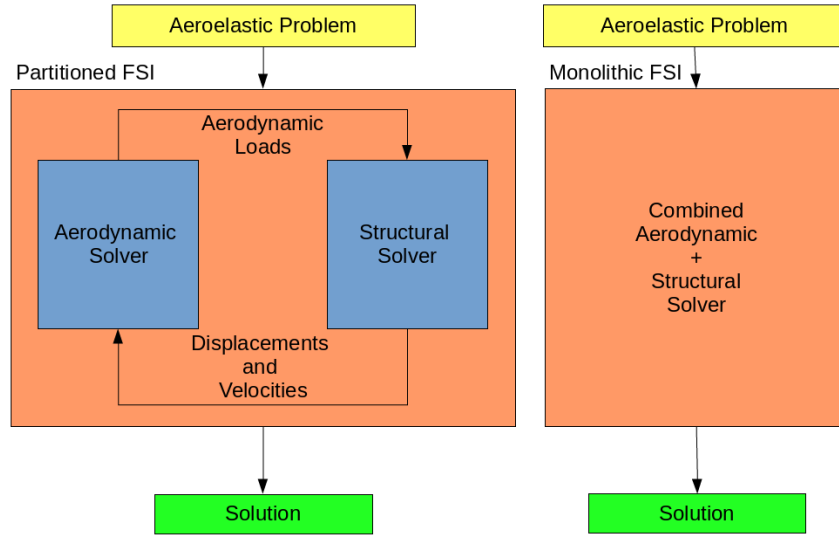
2.1. Aero-structural coupling

Before the airborne wind energy (AWE) sector emerged, soft kites were primarily developed for kitesurfing. In the kitesurfing industry, kite design has followed a Darwinian approach [6], with iterative modifications based on previous models and experimental testing. This approach is based on evolution and experience, and is a time and resource-intensive way to develop new kites. When scaling these kites to AWE systems, there is a desire to simulate the kites' performance to iterate on the kite design before committing to developing a kite in real life.

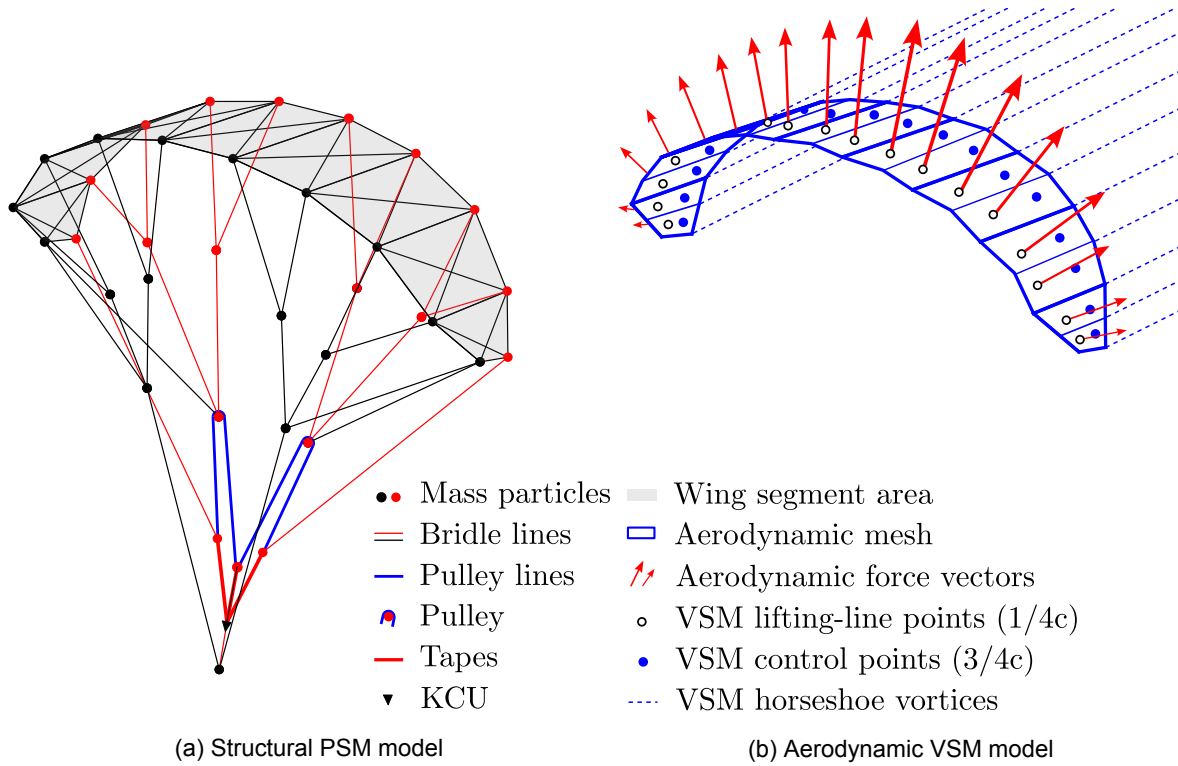
Determining the performance of a soft-wing kite computationally is a non-trivial task. The non-linearities apparent in the kite lead to computationally expensive models. The FSI problem that emerges can be solved with two approaches. The first one is the partitioned approach, where a structural and aerodynamic model is coupled, and both outputs are set up as an input for the other and iterated upon until convergence. Alternatively, one can solve the structural deformation and aerodynamic loads in a single coupled "monolithic" solver. Both methods are visualised in Figure 2.1.

The iterative nature of a partitioned FSI solver leads to a more computationally expensive approach compared to a monolithic FSI solver. However, the setup of a monolithic FSI solver is a lot more complex and less flexible in nature. The advantage of a partitioned solver is in the freedom to vary both models and the ease of developing such models independently. Because of this, the current preference in the AWE sector is the partitioned approach. To ensure a quick convergence time, aerodynamic and structural models are chosen to be as simple as possible while capturing the desired effects.

Multiple structural models and aerodynamic solvers have previously been combined to derive a kite FSI model. Folkersma has modeled ram-air kites [14] and Thedens [41]. Notable attempts for LEI kites are as follows. Breukels [6] modelled a LEI kite by developing a structural and an aerodynamic solver. Bosch [4] developed a different structural model and coupled it to the aerodynamic solver of Breukels. Geschiere [16] adapted Bosch's structural model to include the bridle system. Berens made further improvements on this model [3]. The latest approach for LEI kites [35, 34, 8] forms the basis for this study and features a particle system model (PSM) for the structural part and a vortex step method (VSM) model for the aerodynamics.

**Figure 2.1:** Partitioned and Monolithic FSI methods [27]

Both models are visualized in Figure 2.2. The model is quasi-steady, which means that for a change in aerodynamic load, the static solution of the structural response is used.

**Figure 2.2:** FSI model of the TU Delft V3 Kite [35]

2.2. Deformations

A LEI kite has little rigidity apart from the inflatable struts. The kite shape is enforced by balancing aerodynamic forces and opposing load through the bridle system [19]. A soft-wing kite typically does not steer using the deflection of aerodynamic surfaces, like in an aeroplane. Instead, steering lines are pulled on to deform the kite such that it enters a turn. In aeroplane terminology, this would be similar to a morphing wing. Controlling the angle of attack, or increasing the lift, is done by pulling on the power lines. The same lines can also be used to stall the kite. Both deformation types are shown in Figure 2.3.

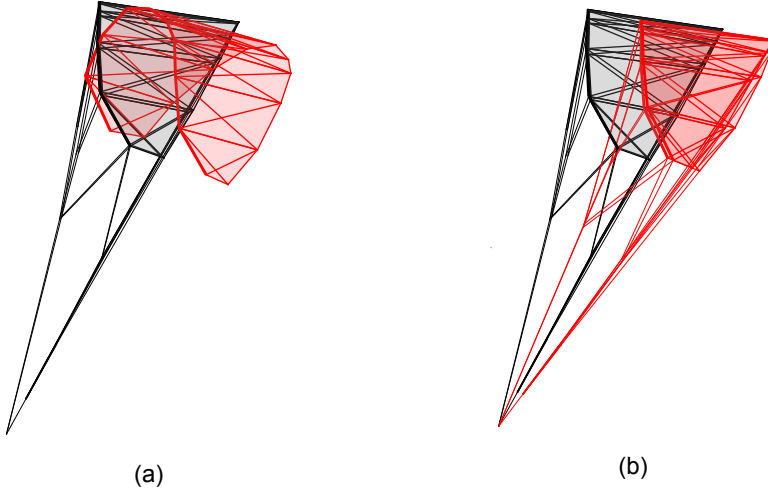


Figure 2.3: Kite deformation due to inputs from the kite control unit [34]. (a) Asymmetric deformation (red) due to a steering input on the kite from the powered state (grey). (b) Depowering of the kite (red) from the powered state (grey)

Asymmetric steering inputs used for steering the kite can lead to difficulty in simulation. Models that are resolved in a quasi-steady manner require an equilibrium point for every time step. Finding such an equilibrium point is challenging due to the inherent instability of the kite. While pitch and yaw are stable, roll is not, and the model is only constrained translationally at the bridle attachment point. As a result, asymmetries like those introduced by a steering input can prevent convergence of the model.

The membranes in the kite also deal with wrinkling effects due to deformations in the canopy. Wrinkling is challenging to capture in a model, and wrinkling models are used to resolve this [40].

2.3. Vibrations

Apart from deformations due to inputs on the bridle lines, kites experience other deformations, some of which are oscillatory. These deformations range from global to local phenomena, varying between small and large timescales. A structural model should be able to replicate the most impactful of these modes, as they can significantly affect kite performance or even cause mission failure. The quasi-steady modelling approach can capture the large-scale deformations [27]. Leuthold [27] gives an overview of the various modes shown in Figure 2.4.

As explained by Leuthold [27], the modes are as follows.

Large-scale deformation modes

- **Bilowing:** The inflation and curvature of the canopy between structural members due to pressure differences. The airfoil shape is affected, and the aerodynamic characteristics

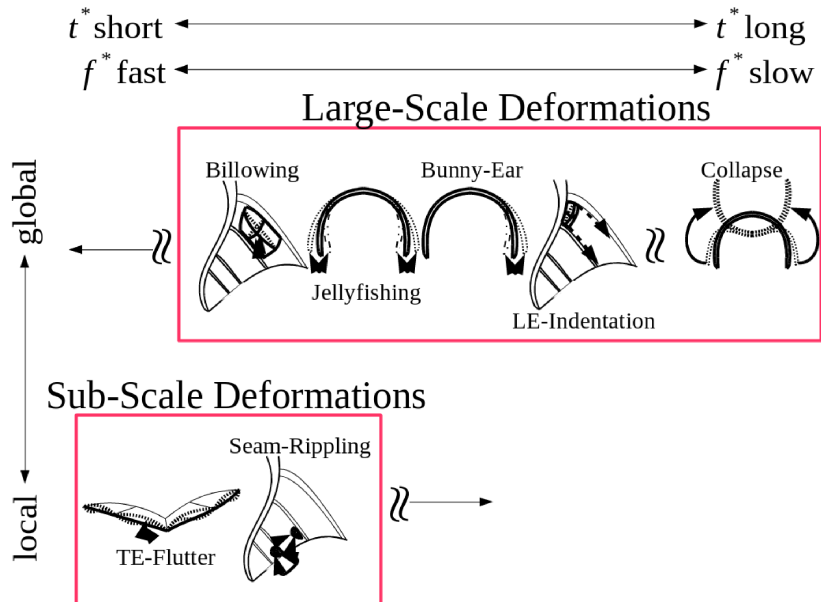


Figure 2.4: Kite deformation modes experienced during a pumping-cycle operation [27]

are also changed.

- **Jellyfishing:** Spanwise oscillatory bending motions resembling the movement of a jellyfish.
- **Bunny-ear:** During a turning motion of the kite, one tip of the kite starts oscillating in and out.
- **Leading edge indentation:** Localized indentation of the leading edge caused by high loads or insufficient inflation pressure. This indentation is the first stage of collapse, but it can still be recovered.
- **Collapse:** Collapse occurs after extreme leading edge indentation. The shape can no longer be maintained, and the kite inverts. When this occurs, there is a high likelihood of crashing the kite.

Sub-scale deformation modes

- **Trailing Edge Flutter:** Trailing Edge Flutter occurs at the trailing edge of the canopy, which starts oscillating due to vortex shedding and causes noise.
- **Seam-Rippling:** Seam rippling is a wave that appears near the trailing edge close to the struts.

Large-scale deformations significantly affect power production, either due to failure or significant changes in the aerodynamics of the kite. As such, it is interesting to see if the FSI model can resolve these. For modelling billowing, the structural model must include a canopy model. Jellyfishing and bunny-ear require modelling the bending and torsional stiffnesses of the inflatable beams. Capturing leading-edge indentation and collapse could be more difficult, as the structure undergoes extreme deformations and requires non-linear modelling. The structural model used by Poland [35], shown in Figure 2.2, does not model deformation of the canopy or bending or torsional stiffness of the struts, and the model can therefore be expanded upon.

2.4. Structural Models

An overview of previously developed models and their advantages and disadvantages is required to identify a suitable model. An overview of the existing models for modelling deformation and their degrees of freedom (DOF) in a LEI kite is given in Figure 2.5. While only an aspect of computational cost and model runtime, higher DOF models typically require more computation.

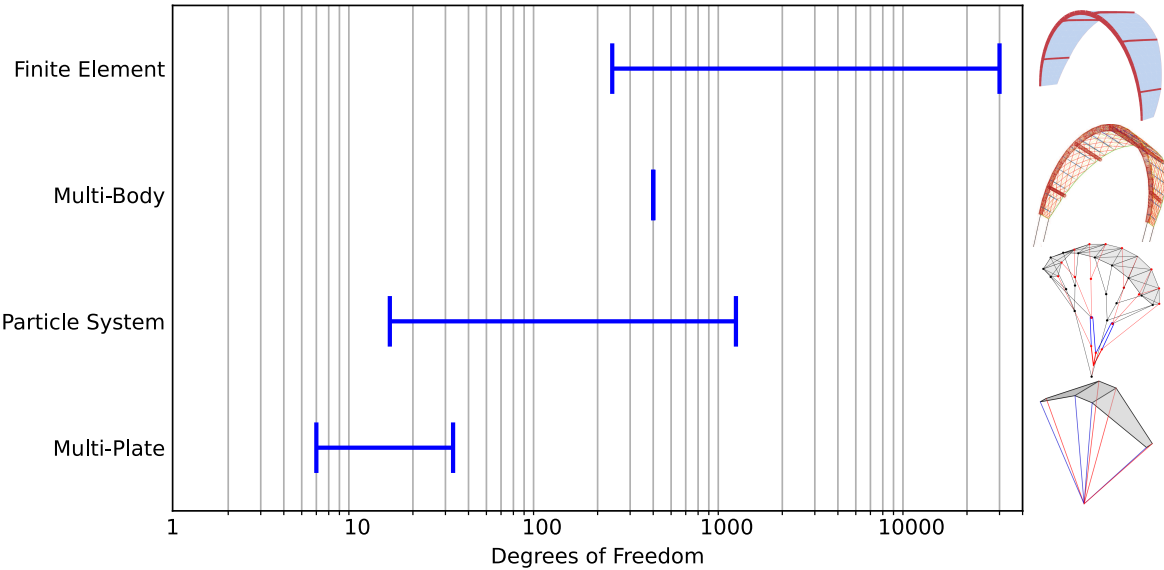


Figure 2.5: Variation in DOF of developed LEI structural model types, model figures from [4, 6, 19]

2.4.1. Models without deformation

Simplified models without deformations are also used to represent a kite. While not useful for an FSI solver, a short description of these types of models is given. A black box model is based on experimental data of a kite and can not be used to model a new kite. A point mass and a rigid body model do not model structural deformation and are therefore too simple for the research.

2.4.2. Multi-plate

Multi-plate models discretise the kite into several plates hinged at the leading edge. This discretisation into multiple plates crudely models the deformation of the kite and the change in centre of gravity, both neglected in rigid kite models [24]. The plates are connected at the leading edge by rotational springs. The model uses non-physical springs, which need to be tuned to build the model. The first multi-plate model was developed by Landsorp et al. [22, 23]. A three plate model was developed for a flight controller by van Til et al. [42]. Later, the V3 kite was modelled with a varying amount of plates for use in FSI by Poland [19], who reported a 2 ms runtime for a seven plate model. However, Poland found the model incompatible with FSI problems due to its inability to deal with asymmetric actuation inputs.

2.4.3. Lumped mass / Particle System

Lumped mass models discretise the kite into multiple particles connected by springs. The first particle-based model for a kite was developed by Furey et al. [15], who modelled a kite with particles and translational springs. The model was coupled to an aerodynamic model to create a flight controller. Later, van der Knaap [21] developed a method to model the bending

stiffness of the inflatable tubes by building pyramid elements from particles and linking them with rotational springs. The method was not implemented to model a kite fully. While the model can resolve bending, the computational time of a rotational spring is about 10 times higher than that of a conventional spring, and by including the required pyramids, the computational cost is 30 times that of a conventional spring [21]. Fechner et.al. developed a more reduced approach for control systems of a kite, modelling a kite with four particles. Geschiere adapted the model [16] by developing a particle-based bridle model, which he coupled to the FSI solver of Bosch [4]. Karadayi [20] applied the model by Fechner et.al. to a rigid-wing kite. Poland [19] also developed a particle system model of the V3 kite. The entire kite and bridle system is modelled as particles and springs. The PSM was later coupled to an aerodynamics solver [35, 8]. While this resulted in a relatively fast model (10s for the kite), the model cannot resolve the inflatable beams' bending stiffness. Furthermore, a PSM has difficulty computing high stiffness elements like tethers, requiring small time steps for convergence.

2.4.4. Multi-body

Breukels [6] developed a kite simulation toolbox in MSC Adams and used a multi-body approach to develop a structural kite model. The leading edge tube and the struts consist of rigid elements hinged and connected with torsional springs. The canopy is modelled with linear springs. As noted by Bosch [4], the limitation of this model is the reliance on artificial elements and parameters without a physical meaning that need to be tuned to simulate the physics of the kite.

2.4.5. Finite Element

Schwoll developed a detailed finite element model (FEM) [37] in the Madymo software. The beams are modelled as pressurised membranes, and the canopy as a membrane. Physical parameters can be used to describe the membranes. Therefore, the model can capture the physics of the kite correctly. The drawback of Schwoll's model is its complexity, consisting of over 30.000 elements. Bosch noted this [4], and therefore developed a reduced finite element model in Matlab. The main reduction in complexity comes from describing the LEI tube and the struts as beam elements. Bosch's method ran approximately 25–30 times slower than real time, with an estimated speed-up factor of 5–10 when switching to a compiled language [4]. Computing power has greatly increased since Bosch's model was developed in 2012. A more reduced method to determine the kite's shape was developed by de Solminihac et.al. [38], who captures all of the kite properties into beam segments. This is a considerable simplification, and while a rapid approach, non-physical parameters have to be tuned to derive the equivalent beam properties. A ram-air kite has been modelled using membrane elements by Thedens [41], who wrote a finite element solver for membranes in Python [40]. The model was coupled to an aerodynamic solver. Declercq made another finite element model for use in FSI [11]. Declercq modelled the V3 kite in Abaqus. Simplifications were made, as the inflatable tubes were modelled as a solid with non-physical material properties. Furthermore, the canopy was thickened to increase convergence. Declercq reported low confidence in the structural model results due to low deformations [11].

2.5. Non-Linear Modelling

2.5.1. Geometric non-linearity

To elaborate on the non-linearity problem of a kite, an example by Bosch [4] is provided in Figure 2.6. A fully horizontal canopy has no stiffness in the vertical direction, as the material can only be stressed in the direction of the fabric. Calculating the deflection from that situation would lead to a very large or infinite deflection. If geometric non-linearity is considered, then

Table 2.1: An overview of structural models for modelling a LEI kite in order of increasing DOFs.

Author	Year	Kite Model	Description	Model DOF*
Lansdorp et al. [22, 23]	2007	Multi-Plate	Two plate model	6
van Til et al. [42]	2018	Multi-Plate	Three plate model for flight control	12
Fechner et al. [12]	2015	Particle System	Four point model for flight control	15
Karadayi [20]	2016	Particle System	Four point model for rigid kites	15
Lansdorp et al. [24]	2008	Multi-Plate	Four plate model for flight control	18
Poland [19]	2022	Multi-Plate	Seven plate model for FSI	33
Furey et al. [15]	2007	Particle System	13 point kite model for flight control	39
Poland [35]	2022	Particle System	37 point model for FSI	111
de Solminihac et.al. [38]	2018	Finite Element	Simplifies entire kite as a spanwise beam	240
Breukels [6]	2011	Multi-Body	Models beams as hinged rigid bodies and the canopy using springs	400
Van der Knaap [21]	2013	Particle System	Derives beam elements using rotational springs. DOF extrapolated to V3 Kite	1122
Bosch [4]	2012	Finite Element	Models the beams as finite elements, and the canopy using shell elements	1332
Schwoll [37]	2012	Finite Element	Models the beams as inflated membranes, and the canopy using membranes	30000
Declerq [11]	2022	Finite Element	Models the kite as a solid, with unphysical material properties	30000

* Not all models have their DOF stated in the reference and are therefore estimated.

the solution would find a deflection that balances the canopy forces with the aerodynamic forces. The solution has to consider that the direction of the canopy stiffness changes due to the change in geometry.

Three frameworks for dealing with geometric non-linearity exist [13].

- **Total Lagrangian Framework:** In the total Lagrangian framework, the equations are formulated with respect to a fixed reference configuration, which does not change during the analysis. Often, this reference configuration is described by the initial configuration.
- **Updated Lagrangian Framework:** The equations for each new step are related to the solution from the previous step. As the simulation moves forward, this starting point is constantly updated to the latest solved shape.
- **Co-rotational Framework:** The element's motion is split into a rigid body motion and a deformational motion. The rigid body motion describes the large-scale translation and rotation of the element in space, while the deformational motion describes the element's change in shape.

The FEM model by Bosch [4] was developed in the Total Lagrangian framework, but notes an interest in using the co-rotational framework. The co-rotational framework can effectively treat problems with large rotations but small strains [13]. This makes it an ideal candidate for developing a model of the kite bridle system and tether. The elements in the aforementioned PyFe3D codebase by Saullo [7] are described using the co-rotational framework.

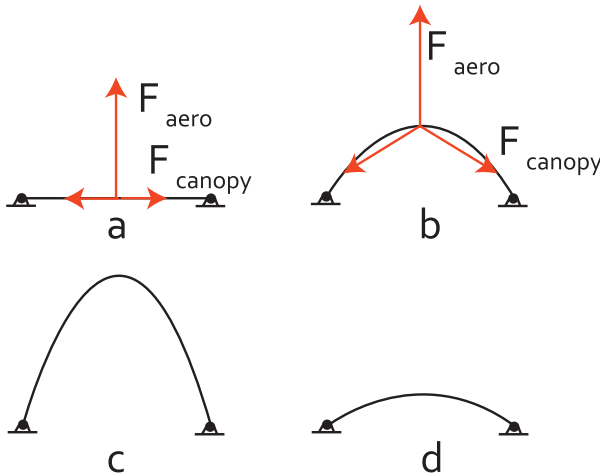


Figure 2.6: Example of geometric non-linear behaviour [4]. (a) Forces in a non-deflected situation. (b) Forces in a deflected situation. (c) Linear deflection. (d) Non-linear deflection

2.5.2. Form Finding

Form finding is a field that is focused on finding the shape of structures and systems and is defined by Veenendaal and Block [43] as follows: "Finding a shape of equilibrium of forces in a given boundary with respect to a certain stress state". Such methods apply directly to the kite deformation problem, as there is a significant geometric non-linearity in the system. Given a structural problem, the form-finding method is interested in finding the static solution of Equation (2.1). The static solution then reduces to Equation (2.2). Since the FSI model to be developed is quasi-steady, the dynamics of the structural model do not need to be included, and a static solution is sufficient.

$$\mathbf{M}\ddot{\mathbf{x}} + \mathbf{C}\dot{\mathbf{x}} + \mathbf{K}\mathbf{x} = \mathbf{P} \quad (2.1)$$

$$\mathbf{K}\mathbf{x} = \mathbf{P} \quad (2.2)$$

The stiffness matrix consists of an elastic part K_e , and optionally, a geometric part K_g . Geometric stiffness takes into account the pre-stressing of a structure. An example of such a situation is when you apply a load onto a ruler in the axial direction. Applying a tension load on a ruler will make it more difficult to bend the ruler. Alternatively, compressing a ruler will make it easier to bend it. When including both elastic and geometric stiffness, Equation (2.3) describes the stiffness matrix of the system.

$$\mathbf{K} = \mathbf{K}_e + \mathbf{K}_g \quad (2.3)$$

Veenendaal and Block have categorised form-finding methods [43] into three categories, as shown in Figure 2.7.

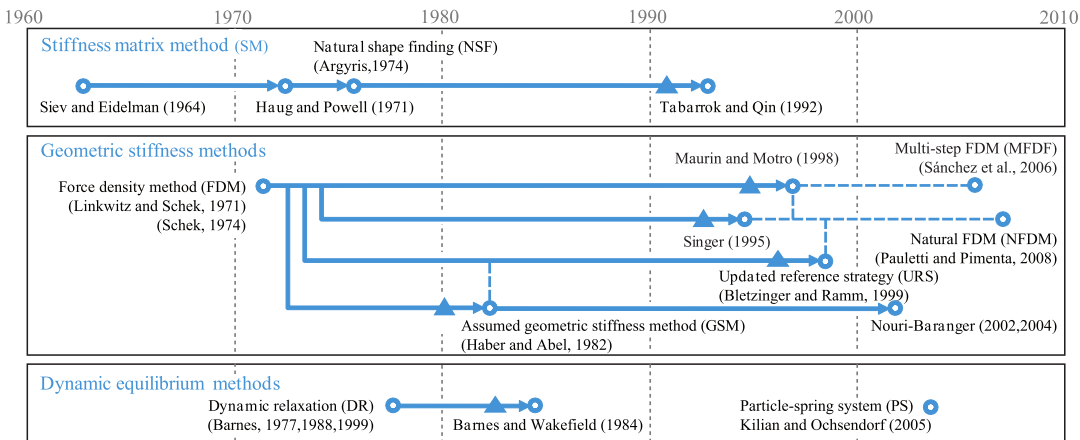


Figure 2.7: Development of various form-finding methods and their respective references, with arrows denoting descendants, dotted lines denoting related but independent methods and triangles denoting a first formulation of surface elements [43]

Stiffness Matrix method

In the stiffness matrix method, one attempts to solve the problem as a structural problem. The system's elastic and geometric stiffness matrix is set up using one of the methods described in Subsection 2.5.1. Then, the stiffness matrix forms a system with the set forces and boundary conditions. The system is then solved for displacements. Geometric non-linearity is solved using the total Lagrangian formulation, updated Lagrangian formulation or the co-rotational formulation [39]. The system can then converge to a solution using Newton-Raphson iteration. Common criticism of the stiffness matrix method is the inclusion of material properties in the equations, which are not explicitly needed to come to a solution and could lead to difficulty in convergence control [1, 18, 30].

Geometric stiffness method

As the name implies, geometric stiffness methods focus on finding a solution using only the geometric stiffness while disregarding the elastic stiffness. The first method developed was the force density method. Force densities and geometric stiffnesses are not intuitive properties. Therefore, they might be challenging to work with [18, 30]. Furthermore, the linear form of the method is only applicable to preliminary results [1] as the linear results depend on mesh density and anisotropy [43].

Dynamic Equilibrium method

Dynamic Equilibrium methods reintroduce a mass and damping matrix, arriving again at Equation (2.1). In this case, the mass and damping matrix can be entirely fictional and tuned for convergence. The intermediate values are non-physical, but the system converges to a static solution. Dynamic equilibrium methods require many parameters for stability and convergence [30]. Including non-physical mass and damping matrices could be viewed as a disadvantage. However, these matrices can be tuned to improve convergence and stability and can be viewed as advantageous [2].

2.6. Beam Modelling

2.6.1. Inflatable Beams

Inflatable beam structures are made out of membranes that can carry little load. The structural strength comes from the pre-stressing of the membrane due to internal pressure [46]. As such,

the structural behaviour of inflatable beams is dictated by material, geometry, shape, and loads more so than rigid beams [44]. Inflatable beams can return to their original shape without any elastic deformation. The first part of the stress-strain deflection curve of an inflatable beam is linear, and the beam can be observed to be taut. Once the loading on the beam is such that the pre-stress is counteracted by the loading, wrinkles start to appear and later collapse [10]. Once wrinkling appears, the response is no longer linear. A comparison of a typical stress-strain curve for a conventional beam and an inflatable beam is given in Figure 2.8.

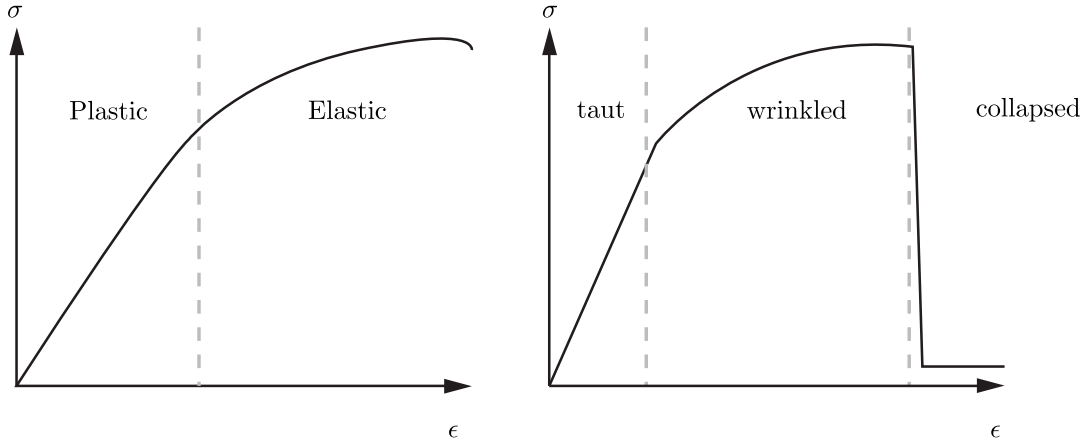


Figure 2.8: Stress-strain curve of a homogenous isotropic beam and an inflated tubular beam [2, 5]

Breukels [6] developed analytical functions for inflatable beam deflection and torsion based on measurements from a test setup. The following relations of a cantilever inflatable beam with a length of 1 m loaded on the tip are found and approached with analytical functions.

$$T = f(p, r, \phi) \quad (2.4)$$

$$F_{\text{tip}} = f(p, r, v) \quad (2.5)$$

Notably, the dependency of the tip load on the deflection leads to a non-constant value of EI , which would be constant throughout a conventional beam.

$$EI(p, r, v) = \frac{F_{\text{tip}}(p, r, v) l^3}{3v} \quad (2.6)$$

Bosch [4] chose a single value for EI to simplify the beam model. This over-predicts the stiffness when dealing with large deflections, and under-predicts the stiffness when dealing with small deflections.

2.6.2. Beam Modelling in FEM

Within FEM, beams can be modelled as conventional Euler-Bernoulli beam elements or Timoshenko beam elements. These elements are typically available in FEM libraries. Therefore, they are simple to implement. Le Van and Wielgosz [25, 26] developed a finite element formulation specifically for modelling inflatable beams. Such an implementation directly makes use of pressure inside the stiffness matrix. Alternatively, one can model an inflatable beam as a membrane with internal pressure [17]. Schwoll's [37] FEM uses this approach. However, such an approach is computationally expensive.

2.6.3. Beam Modelling in PSM

Modelling a beam in a PSM is not an intuitive process, as a linear spring has no bending stiffness. Two approaches are available to model a beam with springs. The first approach is used by van der Knaap [21] as seen in Figure 2.9. Pyramids were formed from particles and connected with stiff springs to form rigid bodies. These were then hinged onto the next pyramid using rotational springs. The rotational springs were tuned such that the beam represents the deflection of a beam.

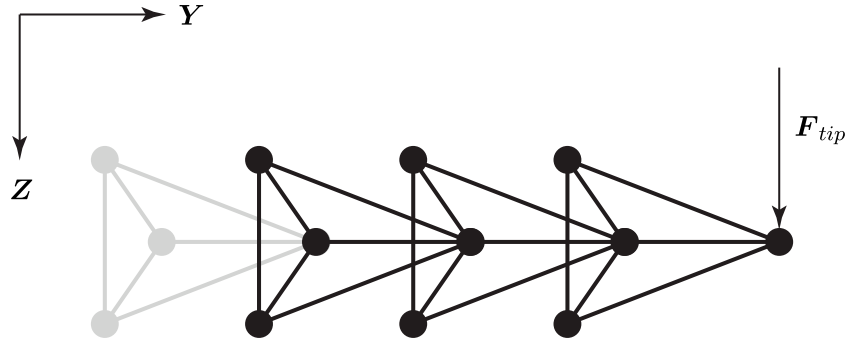


Figure 2.9: Beam representation in a PSM based on rigid pyramids hinged with rotational springs [21].

An alternative approach is to form a truss-like structure from particles and springs. A particle spring assembly can be made and the spring stiffnesses tuned such that the assembly is equivalent to a beam segment [29, 47, 45]. The assembly shown in Figure 2.10 shows an equivalent particle spring assembly consisting of eight particles and 24 springs. The springs were grouped in six stiffnesses, and their values can be determined using energetic equivalence[47]. This means that an equation is set up for all six deformation modes (three axial and three shear). The energy stored in the springs should equal that of the equivalent beam. The energy stored in the beam is derived from the beam properties E and G . The six springs' stiffnesses can then be determined to define the particle system assembly representing a beam segment. A similar approach by Sabzezar et al. [36] describes an equivalent Timoshenko beam for truss structures, again showing the two systems' equivalence.

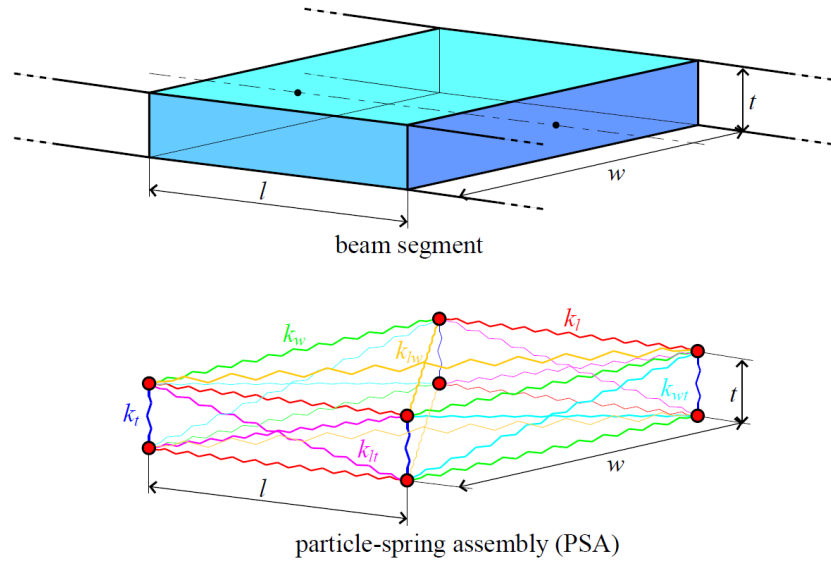


Figure 2.10: Equivalent beam segment and particle spring assembly used to represent a beam in PSM [47, 45]

2.7. Research objective and questions

This literature study analyses the challenges and methods for the structural modelling of LEI kites used in AWE. The challenge in modelling a LEI kite lies in the flexible nature of the kite, leading to a significant coupling between aerodynamic loads and structural deformation. A kite's various deformations and vibrations are discussed, and the large-scale deformations are deemed important to resolve for a good power production estimation. Existing structural models of LEI kites are shared, and their advantages and limitations are discussed. A review of the current models shows a distinct trade-off between computational speed and physical accuracy. With an interest in including bending and torsion of the inflatable beams into the model, two options for new models are selected. A high-fidelity PSM and a low-fidelity FEM are identified as competitive options moving forward, and the methodology of implementing bending stiffness in both is discussed.

The research objective of the thesis is set as follows:

What modelling approach enables a computationally efficient structural model for leading-edge inflatable kites that captures the inflatable structure's bending and torsional stiffness?

Accompanying the objective, the following research (sub)questions are addressed in the study.

1. Which framework is most suitable for developing a LEI kite structural model?
 - (a) How can a beam be modelled in a PSM and applied to a LEI kite?
 - (b) How can a non-linear FEM be set up for a LEI kite?
2. How can the structural model be coupled to the FSI framework?
3. To what extent can the developed method resolve large-scale kite deformations?
4. How does the model compare to in-flight measurements?

3

Modelling Approach

3.1. Aero-structural model

The partitioned aero-structural model developed by Poland and Cayon [35, 34, 8] will be adapted to include the newly developed structural model. Figure 3.1 shows how the aero-structural problem is solved iteratively by feeding the output from the structural model into the aerodynamic model, and vice versa, until convergence. The inputs for the model are:

- Steering and power input:** The lengths of the steering lines and power lines are set as an input, such that one can vary them and see the corresponding aero-structural response.
- Surfplan model:** Surfplan is a modelling software for kites. The model is fed through surfplan adapter [32], which prepares geometrical and aerodynamic inputs to use in the structural and aerodynamic model.
- Apparent velocity:** The velocity seen by the kite is used as an input for the aerodynamic model to determine the aerodynamic loading.

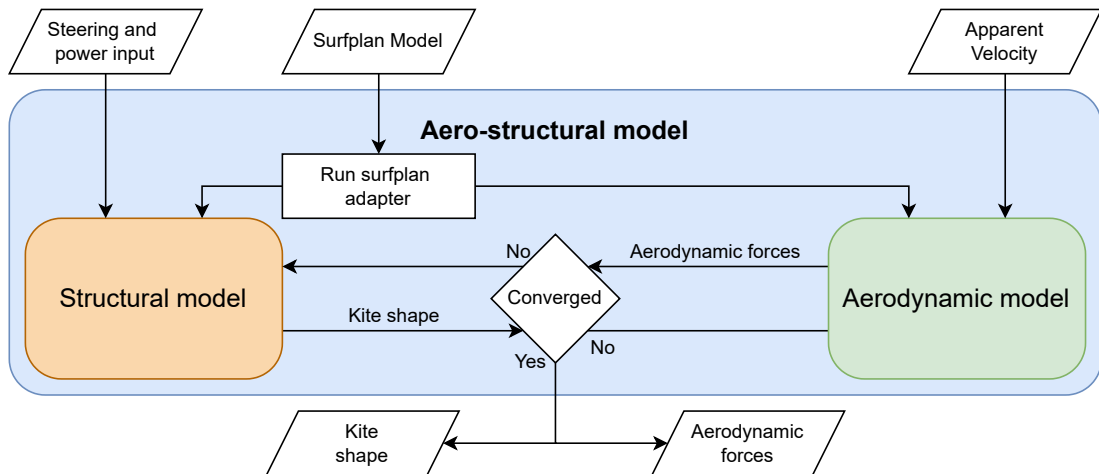


Figure 3.1: Schematic overview of the partitioned aero-structural model

As an output, the kite shape and aerodynamic forces are given. However, one can choose to include more details from the structural and aerodynamic models. The partitioned nature of the model allows for switching between different structural and aerodynamic models. The de-

veloped structural model can therefore be inserted in place of the previous model by matching its inputs and outputs with those of the previous model.

3.2. Structural model

A FEM is developed to fit into the structural model slot in the partitioned aero-structural model. The FEM employs the CRF to address the non-linear geometry. The system is solved using the Newton-Raphson method. An overview of the model is given in Figure 3.2

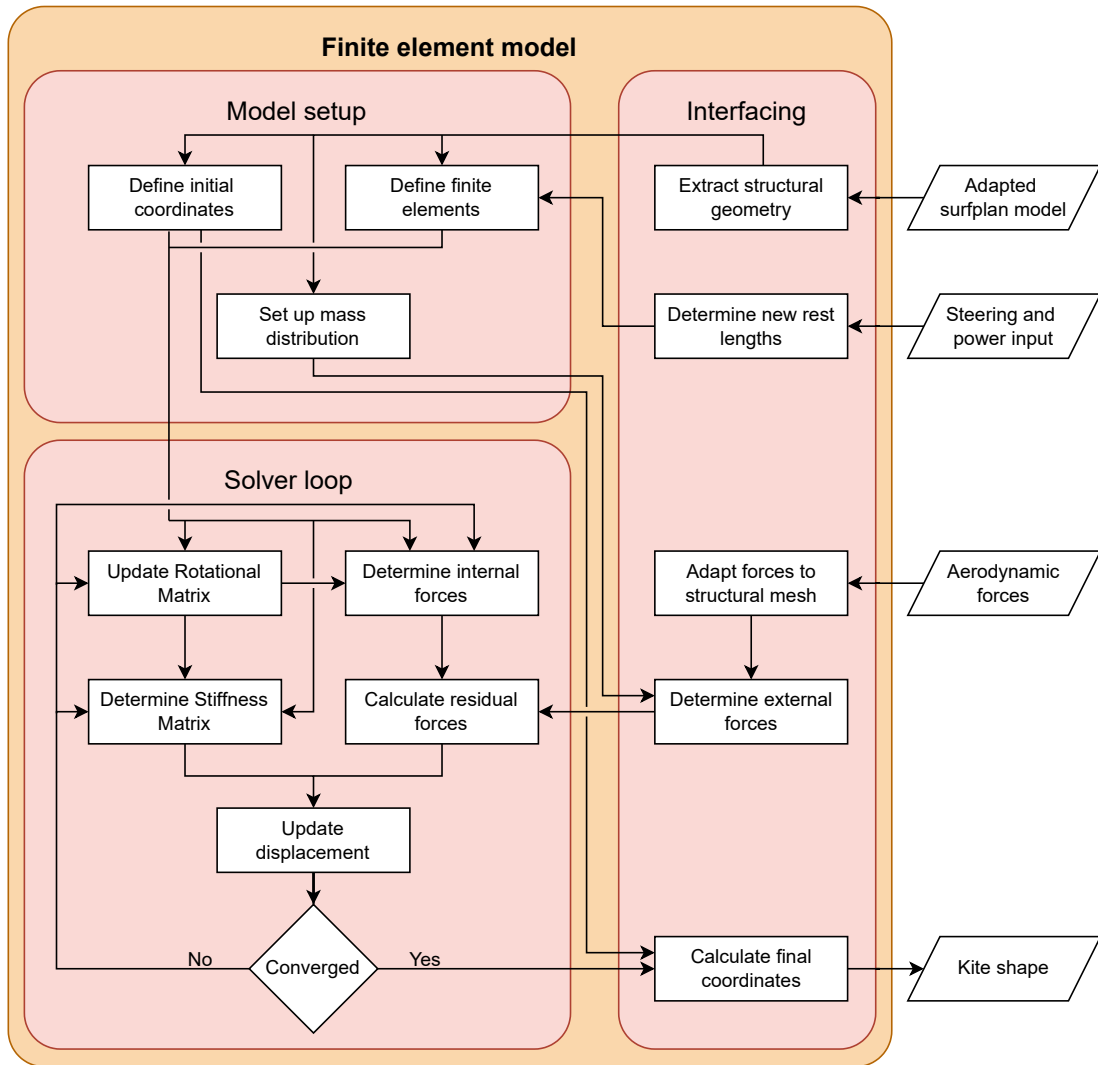


Figure 3.2: Schematic overview of the finite element model

The model can be set up using the adapted surfplan geometry files, and optionally, the lengths of the steering and power tapes can be adjusted. The model is set up such that all finite elements are defined, all nodal coordinates are defined, and the mass is distributed along the nodes. Then, one can input an aerodynamic loading, which will be used to determine the external forces. Within the Newton-Raphson iteration loop, the displacement iterates towards a position where the internal forces and external forces at each node are balanced. In line with the CRF, the rotational matrix is updated each iteration to track the orientation of individual

elements. The stiffness matrix and residual force vector are also set up at each iteration. The displacement is then updated by solving the linear system $\mathbf{K}\Delta\mathbf{u} = \mathbf{r}$. When the normalised residual force vector is below the convergence criteria, the displacement is outputted and added to the initial coordinates to provide the final kite shape.

3.3. Aerodynamic model

The vortex-step method is used as the aerodynamic model. This model, developed by Cayon [8], iteratively determines the circulation distribution over the kite's segments. The model is already integrated in the aerostructural loop and will not be modified. An overview of the VSM is provided in Figure 3.3.

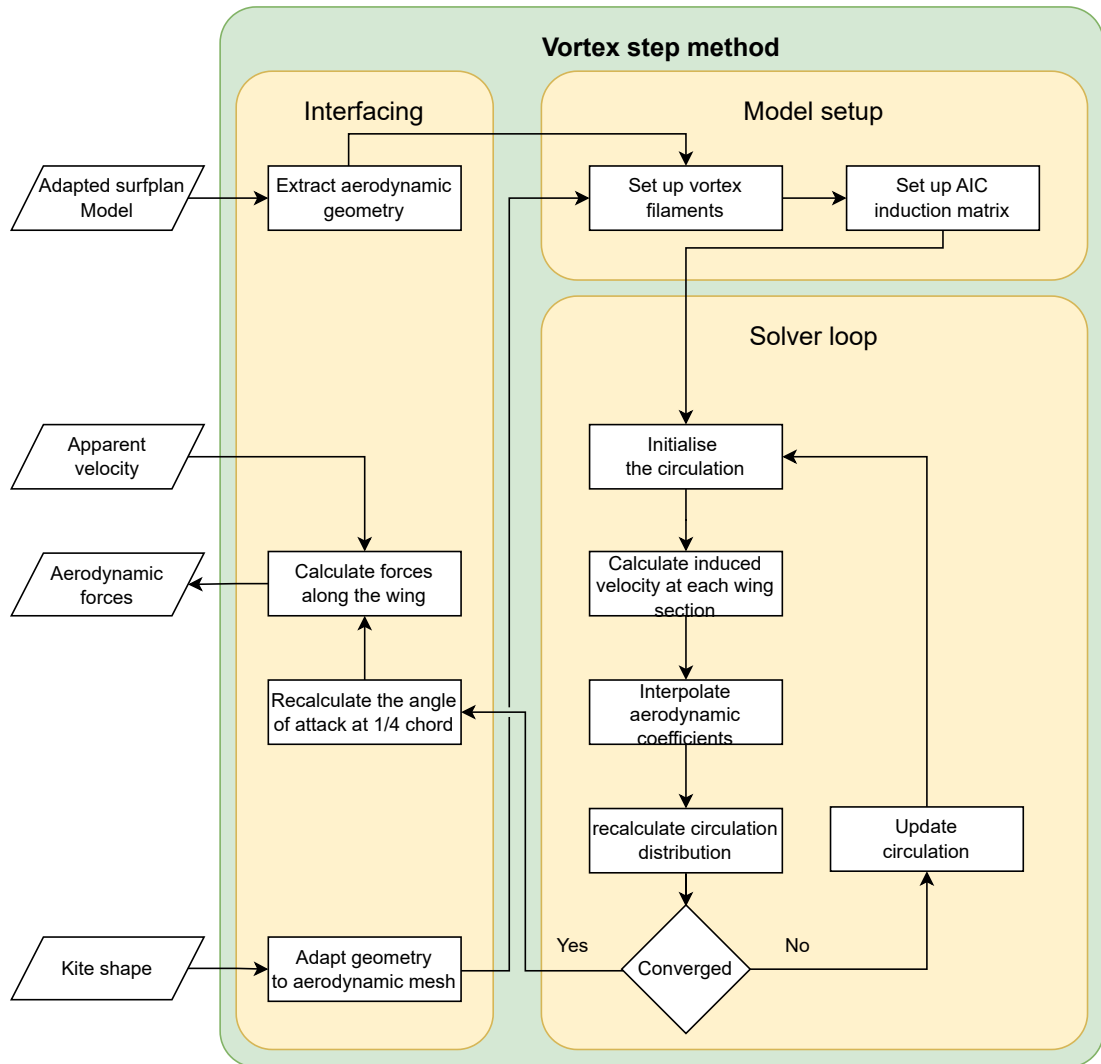


Figure 3.3: Schematic overview of the vortex step method

4

Finite element framework for kites

4.1. Finite element formulation

The framework presented in this chapter shows how one can discretise the different parts of a kite into finite elements. The framework makes use of two node elements, existing in a three-dimensional space. Figure 4.1 shows an element spanning between nodes n_1 and n_2 . Each node has three translational and three rotational degrees of freedom (DOF). In total a two node element has 12 DOF, the displacement vector in the element coordinate system is shown in Equation (4.1). A stiffness matrix, \mathbf{K}^e , of dimensions 12×12 is accompanied with each element.

$$\mathbf{u}^{e,T} = [u_1 \ v_1 \ w_1 \ \varphi_1 \ \theta_1 \ \psi_1 \ u_2 \ v_2 \ w_2 \ \varphi_2 \ \theta_2 \ \psi_2] \quad (4.1)$$

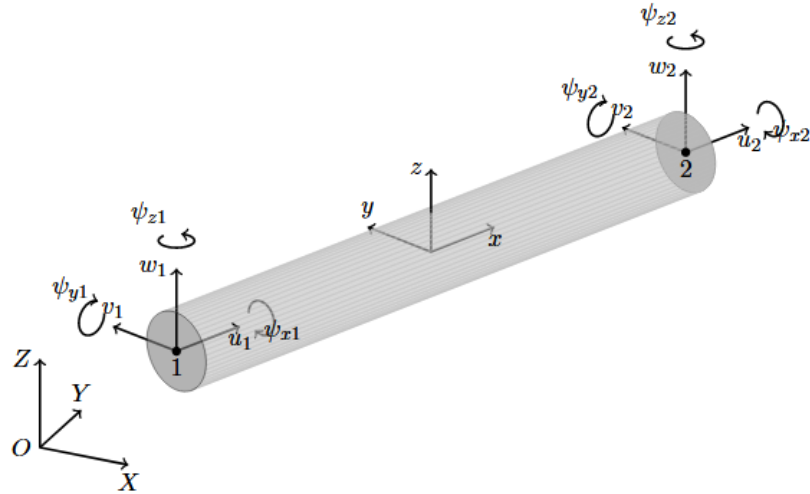


Figure 4.1: A two node element in three-dimensional space with six DOF per node, accompanied by a local coordinate system [4] TODO: replace by own figure

Each element has a local coordinate system, with the x axis defined in the element's direction (x, y, z)^e. The element is placed within a global coordinate system (x, y, z)^g TODO: check with bathe. The element's coordinate frame may be misaligned with the global coordinate

frame's orientation. Three rotations can be performed to align the element axes with the global axes. These three rotations can be seen in Figure 4.2.

Todo: is this euler rotation?

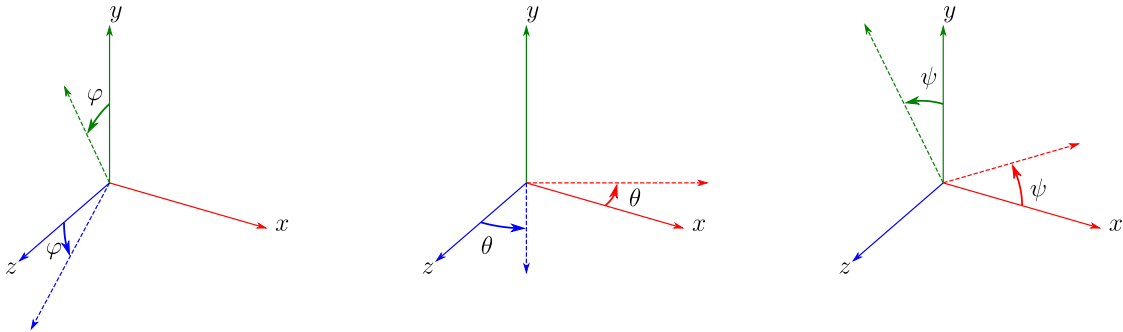


Figure 4.2: Coordinate system rotations around the *x*, *y* and *z* axes.

TODO : explain how to map *x* coordinates plus deflections to rotations

These rotations lead to the coordinate system rotation matrix \mathbf{T}_m which maps from the element to global coordinate system.

$$\mathbf{T} = \begin{bmatrix} 1 & 0 & 0 \\ 0 & \cos \varphi & -\sin \varphi \\ 0 & \sin \varphi & \cos \varphi \end{bmatrix} \begin{bmatrix} \cos \theta & 0 & \sin \theta \\ 0 & 1 & 0 \\ -\sin \theta & 0 & \cos \theta \end{bmatrix} \begin{bmatrix} \cos \psi & -\sin \psi & 0 \\ \sin \psi & \cos \psi & 0 \\ 0 & 0 & 1 \end{bmatrix} \quad (4.2)$$

$$\mathbf{T} = \begin{bmatrix} \cos \psi \cos \theta & -\sin \psi \cos \varphi + \cos \psi \sin \theta \sin \varphi & \sin \psi \sin \theta + \cos \psi \sin \theta \cos \varphi \\ \sin \psi \cos \theta & \cos \psi \cos \varphi + \sin \psi \sin \theta \sin \varphi & -\cos \psi \sin \varphi + \sin \psi \sin \theta \cos \varphi \\ -\sin \theta & \cos \theta \sin \varphi & \cos \theta \cos \varphi \end{bmatrix} \quad (4.3)$$

The rotation matrix \mathbf{R} is used to map element displacements, forces and the stiffness matrix to the global coordinate frame, and the inverse \mathbf{R}^{-1} is used to map from the global to element coordinate frame.

$$\mathbf{R} = \begin{bmatrix} \mathbf{T} & 0 & 0 & 0 \\ 0 & \mathbf{T} & 0 & 0 \\ 0 & 0 & \mathbf{T} & 0 \\ 0 & 0 & 0 & \mathbf{T} \end{bmatrix} \quad (4.4)$$

Thus, the element contribution to the global coordinate system can be written as.

$$\mathbf{u}^g = \mathbf{R}\mathbf{u}^e \quad (4.5)$$

$$\mathbf{f}^g = \mathbf{R}\mathbf{f}^e \quad (4.6)$$

The linear displacement of an element due to a force vector \mathbf{f}^e in the element coordinate system can be obtained by solving the system

$$\mathbf{K}^e \mathbf{u}^e = \mathbf{f}^e \quad (4.7)$$

Applying Equation (4.5) and Equation (4.6) to Equation (4.7) leads to.

$$\mathbf{K}^g \mathbf{u}^g = \mathbf{f}^g \quad (4.8)$$

Where the local contribution to the global stiffness matrix is given by

$$\mathbf{K}^g = \mathbf{R}^T \mathbf{K}^e \mathbf{R} \quad (4.9)$$

In a system consisting of more elements, a stiffness matrix needs to be assembled from the individual elements' contribution. Therefore, the individual contribution of the element between n_1 and n_2 is now denoted as \mathbf{K}_{12}^g . Similarly, an element between n_1 and n_3 is denoted as \mathbf{K}_{13}^g . The individual contribution of these elements take the form of

$$\mathbf{K}_{12}^g = \begin{bmatrix} \mathbf{K}_{11} & \mathbf{K}_{12} \\ \mathbf{K}_{21} & \mathbf{K}_{22} \end{bmatrix} \quad (4.10)$$

$$\mathbf{K}_{13}^g = \begin{bmatrix} \mathbf{K}_{11} & \mathbf{K}_{13} \\ \mathbf{K}_{31} & \mathbf{K}_{33} \end{bmatrix} \quad (4.11)$$

where each sub-matrix has a dimension of 6×6 . For a system of n nodes $\{n_1, n_2, \dots, n_n\}$ the assembled global stiffness matrix has the form of

$$\mathbf{K} = \begin{bmatrix} \mathbf{K}_{11} & \mathbf{K}_{12} & \mathbf{K}_{13} & \cdots & \mathbf{K}_{1n} \\ \mathbf{K}_{21} & \mathbf{K}_{22} & \mathbf{K}_{23} & \cdots & \mathbf{K}_{2n} \\ \mathbf{K}_{31} & \mathbf{K}_{32} & \mathbf{K}_{33} & \cdots & \mathbf{K}_{3n} \\ \vdots & \vdots & \vdots & \ddots & \vdots \\ \mathbf{K}_{n1} & \mathbf{K}_{n2} & \mathbf{K}_{n3} & \cdots & \mathbf{K}_{nn} \end{bmatrix} \quad (4.12)$$

Again, the sub-matrices are of dimensions 6×6 . The total global stiffness matrix is assembled by adding all elements' contribution to the system. The element between n_1 and n_2 adds contributions to \mathbf{K}_{11} , \mathbf{K}_{12} , \mathbf{K}_{21} and \mathbf{K}_{22} of Equation (4.12). Similarly, the element between n_1 and n_3 contributes to \mathbf{K}_{11} , \mathbf{K}_{13} , \mathbf{K}_{31} and \mathbf{K}_{33} . The assembled global system is then described by

$$\mathbf{K}\mathbf{u} = \mathbf{f} \quad (4.13)$$

With the method described in this section, one can derive the assembled stiffness matrix of any system consisting of n nodes in three-dimensional space, with an arbitrary amount of two node elements. The global system can be solved for displacements based on a force vector \mathbf{f} . A DOF can be fixed by setting the corresponding displacement to 0 and removing the corresponding column and row from the matrices and vectors before solving Equation (4.13).

One can see that the rotation matrix is a function of the displacement of the nodes, and therefore the assembled stiffness matrix is as well, i.e. $\mathbf{R}(\mathbf{u})$ and $\mathbf{K}(\mathbf{u})$.

4.2. Kite-specific elements

4.2.1. Bridle line system

The kite is attached to the tether through the bridle line system. The bridle line system enforces the shape of the kite, which is needed to provide lift. The aerodynamic load is transferred through the bridle line system to the tether, which transfers the load to the ground. For AWE applications, bridle line systems are often complex with multiple connection points on the kite, pulleys, and knots in the lines. Furthermore, the steering lines are shortened or lengthened to deform the kite for steering, and the power line is used to increase the angle of attack of the kite. Figure 5.2 shows the bridle line system of the V3 kite. The bridle lines exhibit relatively small deformations but significant rotations. Therefore, they are ideal to model with FEM using the CRF.

the bridle lines and pulleys are modelled as spring elements. A spring element can only transfer force along its elongation axis, which aligns with the local x-axis. Therefore, its stiffness matrix is simple and consists solely of a spring stiffness k_x .

$$\mathbf{K}^e = \begin{bmatrix} \mathbf{K}_{11}^e & \mathbf{K}_{12}^e \\ \mathbf{K}_{21}^e & \mathbf{K}_{22}^e \end{bmatrix} \quad (4.14)$$

$$\mathbf{K}_{11}^e = \mathbf{K}_{22}^e = -\mathbf{K}_{21}^e = -\mathbf{K}_{12}^e = \begin{bmatrix} k_x & 0 & 0 & 0 & 0 & 0 \\ 0 & 0 & 0 & 0 & 0 & 0 \\ 0 & 0 & 0 & 0 & 0 & 0 \\ 0 & 0 & 0 & 0 & 0 & 0 \\ 0 & 0 & 0 & 0 & 0 & 0 \\ 0 & 0 & 0 & 0 & 0 & 0 \end{bmatrix} \quad (4.15)$$

For a non-compressive spring, the spring stiffness is set to 0 and back to k_x again based on the current length of the spring.

$$k_x = \begin{cases} k_x & \text{if } (l - l_0) \geq 0, \\ 0 & \text{if } (l - l_0) < 0 \end{cases} \quad (4.16)$$

The bridle lines can be slack and are therefore modelled as non-compressive springs. Each endpoint of a spring is then a knot, and can be used to attach more lines. Therefore, a bridle line system essentially becomes a combination of non-compressive springs, where each connection point has 3 degrees of freedom.

The bridle lines are generally made from high-performance materials such as Dyneema, which leads to stiff bridle lines. The spring stiffness used in the model is not representative of the Dyneema material. Using the material properties leads to a stiff system that is difficult to solve. This increases computational costs and affects stability. Therefore, lower stiffnesses are used and tuned so that the final elongation is less than 1%.

A connection of two nodes is shown in Figure 4.3. This spring spans between n_1 and n_2 . The spring has a length of l_{12} and a corresponding rest length l_0 .

The internal force in the element coordinate frame is then calculated by Equation (4.17), where the value k_x is again adapted to represent a non-compressive spring.

$$\mathbf{f}_{int}^{e,T} = [k_x(l - l_0) \quad 0 \quad 0 \quad 0 \quad 0 \quad 0] \quad (4.17)$$

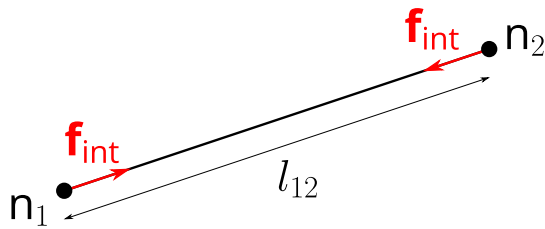


Figure 4.3: Internal forces of a line between n_1 and n_2

The internal force of the element is then transformed to the global coordinate frame and applied to each node.

$$\mathbf{f}_{int}^g = \mathbf{R}\mathbf{f}_{int}^e \quad (4.18)$$

A pulley is modelled as a combination of spring elements. Figure 4.4 shows a pulley between nodes n_1 , n_2 and n_3 . The pulley consists of two spring elements, one between n_1 and n_2 , and one between n_2 and n_3 . Node n_2 is the pulley node and is free to move across the line. In order to link the two elements into a pulley, the internal force calculation is unified. The total length of the two elements, $l_{123} = l_{12} + l_{23}$ is used in Equation (4.16) and Equation (4.17). The two elements also share the same k_x and l_0 . This leads to the same magnitude of \mathbf{f}_{int} across the two elements. By linking these properties node n_2 can move such that l_{12} is shortened and l_{23} lengthened, and vice versa.

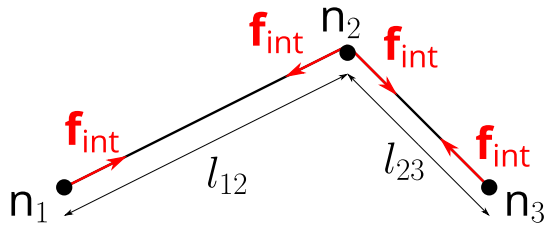


Figure 4.4: Internal forces of a pulley between n_1 , n_2 and n_3 , where n_2 is the pulley node

For a network of nodes $\{n_1, n_2, \dots, n_n\}$, spring connections and pulley connections the internal forces at each node can be determined based on the position of the nodes. Therefore, the internal force vector is a function of the deflection of the system, i.e. $\mathbf{f}_{int}(\mathbf{u})$.

4.2.2. Leading edge and struts

The leading edge tube and struts of a kite are inflatable structures that provide bending and torsional stiffness due to an overpressure inside the tube. They are used to enforce the aerodynamic shape of the kite and therefore play a vital role. Furthermore, the leading edge tube also acts as a circular leading edge, defining the aerodynamics over the chord. The inflatable structures can be modelled as beam elements, which are two-node elements with 12 DOF,

three translational and three rotational per node. The advantage of using beam elements is that the complexity is significantly reduced compared to the alternative option, which involves modelling the inflatable structures as membranes with internal pressure. A beam element relies on material properties and surface cross-section properties to determine the stiffness matrix. The stiffness matrix formulation for a Timoshenko beam element by Luo [28] is used, who describes the explicit expression of the full 12×12 stiffness matrix. The stiffness matrix is a function of beam properties and cross-section properties.

$$\mathbf{K}^e(E, G, A, I_y, I_z, k, L) \quad (4.19)$$

For a circular beam the following holds

$$A = \pi r^2 \quad (4.20)$$

$$I = I_z = I_y \frac{\pi r^4}{4} \quad (4.21)$$

$$k = \frac{8}{9} \quad (4.22)$$

Thus, all cross-sectional properties rely on r , and k is a constant.

$$\mathbf{K}^e(E, G, r, L) \quad (4.23)$$

Material properties E and G are not directly obtainable for inflatable beams, as the stiffness is dependent on the pressure. Instead, fitted equations by Breukels [6] are used to match the properties of inflatable beams to typical material properties, E and G . Breukels performed bending and torsion experiments on inflatable cantilevered beams of $L = 1$ m and derived the following fitted equations to relate deflection with tip force, and rotation with torque.

$$P(p, r, \delta) = (C_1 r + C_2)p^2 + (C_3 r^3 + C_4) \left(1 - e^{-\frac{(C_5 r^5 + C_6)p + (C_7 r + C_8)}{C_1 r + C_2} \delta} \right) \quad (4.24)$$

$$T(p, r, \varphi) = ((C_{13}r + C_{14})p + (C_{15}r + C_{16})) \tan^{-1}((C_{17}r^4 \ln(p) + (C_{18}r^3 + C_{19})\varphi) \quad (4.25)$$

from Timoshenko beam theory the following relations link rotation and deflection with beam properties E and G .

$$\delta = \frac{PL^3}{3EI} + \frac{PL}{kGA} \quad (4.26)$$

$$\varphi = \frac{TL}{GJ} = \frac{TL}{2GI} \quad (4.27)$$

Therefore, E and G can be expressed as:

$$E = \frac{PL^3}{3I(\delta - \frac{PL}{kAG})} \quad (4.28)$$

$$G = \frac{TL}{2\varphi I} \quad (4.29)$$

Breukel's equations for a beam of $L = 1$ m from Equation (4.24) and Equation (4.25) can then be inserted leading to the relations

$$E(p, r, \delta, \varphi, k) = \frac{P(p, r, \delta)}{3I(\delta - \frac{P(p, r, \delta)}{kAG})} \quad (4.30)$$

$$G(p, r, \varphi) = \frac{T(p, r, \varphi)}{2\varphi I} \quad (4.31)$$

The element stiffness matrix can now be defined with p , δ , and φ , instead of E and G .

$$\mathbf{K}^e(p, r, L, \delta, \varphi) \quad (4.32)$$

The stiffness of the element is not linear and varies with deflection and rotation, and should be updated at each iteration. Therefore, the deflection and rotation must also be updated at each iteration as the element displacement vector \mathbf{u}^e , given in Equation (4.1), changes.

$$\delta = S_\delta \left\| \begin{bmatrix} u_2 \\ v_2 \end{bmatrix} - \begin{bmatrix} u_1 \\ v_1 \end{bmatrix} \right\| \quad (4.33)$$

$$\varphi = S_\varphi |\varphi_2 - \varphi_1| \quad (4.34)$$

Here, S_δ and S_φ are scaling factors to scale the deflection and rotation of an element with length L to that of an element of $L = 1$ m, as that is the input required for Breukels' equations. Deflection in a Timoshenko beam scales both with L and L^3 , as can be seen in Equation (4.26). The linear part is associated with shear deformation, and the cubic part is associated with bending deformation. To scale element deflections, it is assumed that shear deformation is dominant. This assumption will hold for short elements but will no longer be valid for longer elements. The limits have been investigated and are shared in Subsection 4.4.3. For scaling of rotations, a linear relation is also used, which is directly derived from Equation (4.27).

$$S_\delta = \frac{\delta(L=1)}{\delta(L=L)} \approx \frac{1}{L} \quad (4.35)$$

$$S_\varphi = \frac{\varphi(L=1)}{\varphi(L=L)} = \frac{1}{L} \quad (4.36)$$

Now, the element stiffness matrix can be set up using pressure, radius, element length, and nodal displacements.

$$\mathbf{K}^e(p, r, L, \mathbf{u}^e) \quad (4.37)$$

which can be transferred to the global stiffness matrix as described in Section 4.1. The internal forces of a beam element are derived using the element stiffness matrix and element displacement.

$$\mathbf{f}_{\text{int}}^e = \mathbf{K}^e \mathbf{u}^e \quad (4.38)$$

4.2.3. Canopy

The goal of modelling the canopy is to capture the global deformation caused by translations, rotations, and element deformation. Part of the canopy of the kite can be modelled by combining four nodes with six non-compressive springs. The membrane material properties are not directly modelled, but are assumed to be very stiff, as the main contribution to the global deformation is due to element translation and rotation. Each non-compressive spring is therefore modelled with high stiffness, such that the elongation falls within one percent of its original length. Figure 4.5(a) shows how four nodes and six non-compressive springs are combined to represent part of the canopy. Figure 4.5(b) shows how this integrates further into a kite section, where three sides of the canopy are connected to inflatable beams. The inflatable beam lengths may vary. Therefore, the four-node canopy sections are not square, but quadrilateral. Each node that is not connected to an inflatable beam has no rotational stiffness, and therefore, the canopy sections can hinge around these points.

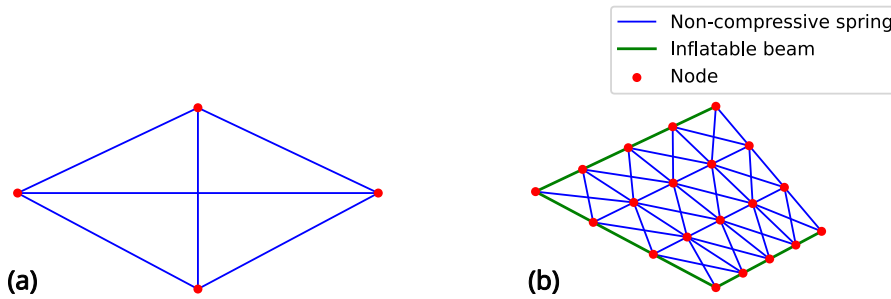


Figure 4.5: (a) Quadrilateral representation of part of a canopy. (b) Example of canopy discretisation within a kite segment

4.3. Newton-Raphson iteration

To get the linear response to a force vector \mathbf{f}_{ext} , only the initial coordinates and element definitions are required and the displacements can be derived from that. The kite has geometric and material non-linearities, which can not be derived linearly. An iterative approach is required to converge to the solution. Each iteration, the geometry, the material properties and internal forces are all adapted to the displacement \mathbf{u} . The Newton-Raphson iteration scheme, presented in Algorithm 1 is used to converge to the solution. Each iteration, all elements' rotational matrices are updated according to the method provided in Section 4.1, using the initial displacement vector, which can be set to zero. The internal forces are calculated with respect to that displacement, as explained in Section 4.2. Then using the external force vector, the residual vector can be determined. The stiffness matrix is also recalculated each iteration based on the current displacement guess. The linear displacement solution is then added to the guess, and the loop restarts until the residual value is converged.

Algorithm 1 Newton–Raphson iteration for geometrically non-linear FEM

Input: Initial guess displacement \mathbf{u}^0 , tolerance ε , maximum iterations i_{\max} , external force vector \mathbf{f}_{ext} , element definitions

Output: Nodal displacement \mathbf{u}

- 1: $i = 0$
- 2: **while** $i < i_{\max}$ **do**
- 3: Update each elements' rotational matrix $\mathbf{R}(\mathbf{u}^i)$
- 4: Assemble internal force vector $\mathbf{f}_{\text{int}}(\mathbf{u}^i)$
- 5: Assemble residual vector $\mathbf{r}(\mathbf{u}^i) = \mathbf{f}_{\text{ext}} - \mathbf{f}_{\text{int}}(\mathbf{u}^i)$
- 6: Assemble stiffness matrix $\mathbf{K}(\mathbf{u}^i)$ ▷ Elements updated using CRF
- 7: Solve linear system: $\mathbf{K}(\mathbf{u}^i)\Delta\mathbf{u}^i = \mathbf{r}(\mathbf{u}^i)$ ▷ Stiffness matrix acts as Jacobian
- 8: Update solution: $\mathbf{u}^{i+1} \leftarrow \mathbf{u}^i + \Delta\mathbf{u}^i$ ▷ $\Delta\mathbf{u}^i$ can be limited to help convergence
- 9: **if** $\|\mathbf{R}\| < \varepsilon$ **then**
- 10: **return** \mathbf{u}
- 11: **end if**
- 12: Update iteration: $i \leftarrow i + 1$
- 13: **end while**

4.4. Verification

4.4.1. Saddle problem

The saddle problem is a form-finding problem, where a pre-tensioned spring system is solved to find the equilibrium state. The solution has the form of a mathematical saddle. A square grid is initialized and the border nodes are moved up and down in the z direction. The border nodes are then constrained to form the initial configuration seen in Figure 4.6(a). The system is then solved using the scheme explained in Section 4.3. The result for $\|\mathbf{r}\| < 1e^{-3}\text{N}$ can be seen in Figure 4.6(b).

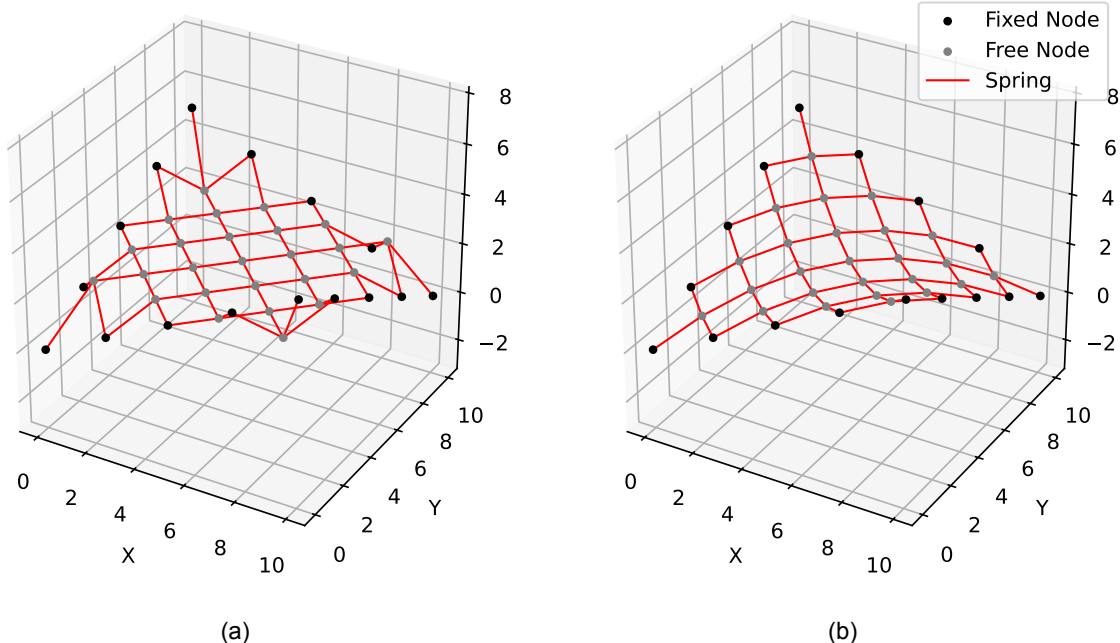


Figure 4.6: (a) Initial conditions of a 5×5 saddle form problem (b) Converged solution of 5×5 saddle form problem.

The saddle problem is also solved using the PSM with the same convergence criteria. The results of varying grid sizes are compared in Table 4.1. For each node, the difference between the converted PSM and FEM solutions were calculated and the maximum is given in the third column. It shows that both models converge to the same solution. Examining the last two columns, the FEM solves the system more efficiently than the PSM. As the grid size increases, the computational time of the PSM increases more rapidly than that of the FEM solver.

Table 4.1: Comparison between FEM and PSM for various saddle problem sizes.

Grid size	Number of nodes	Maximum nodal difference [mm]	FEM solver time [s]*	PSM solver time [s]*
3×3	13	0.06	0.03	0.08
5×5	41	0.10	0.11	0.41
7×7	85	0.16	0.27	1.68
9×9	145	0.27	0.71	2.92
11×11	221	0.38	1.61	5.95
13×13	313	0.49	3.09	18.10

*Using a HP Zbook Power G7 mobile workstation

4.4.2. Nested pulleys

Three pulleys are modelled to verify that the pulley physics are resolved correctly. Four fixed nodes are placed one meter apart. Then, the combinations (n_1, n_5, n_2) and (n_3, n_6, n_4) are set up as pulleys. Furthermore, a pulley system is nested below this with nodes (n_5, n_7, n_6) . All three pulley systems have a rest length of 2.2m A force at a 15° angle from the y axis is applied at n_7 . The resulting initial configuration can be seen in Figure 4.7(a). The system is solved using the scheme from Section 4.3, and the result is seen in Figure 4.7(b). For an ideal, frictionless pulley the angle between the force applied at a node and the two pulley lines should be equal [34]. The angles calculated from the converged state are shown in Table 4.2, and indeed it can be seen that $\alpha_1 = \alpha_2$, $\beta_1 = \beta_2$ and $\gamma_1 = \gamma_2$.

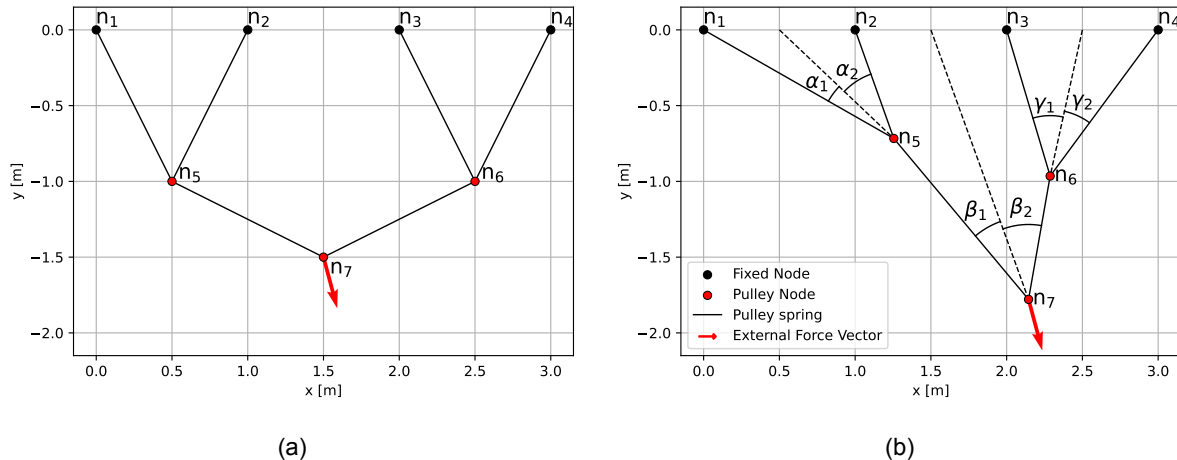


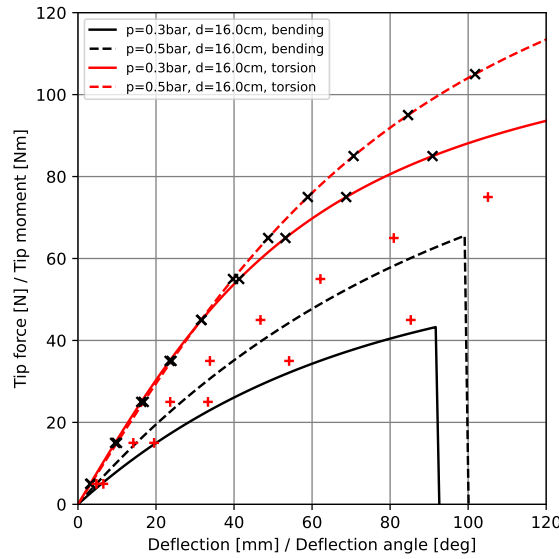
Figure 4.7: (a) Initial conditions of a nested pulley system (b) Converged solution of the nested pulley system.

Table 4.2: Pulley line angles from converged state of the nested pulley system

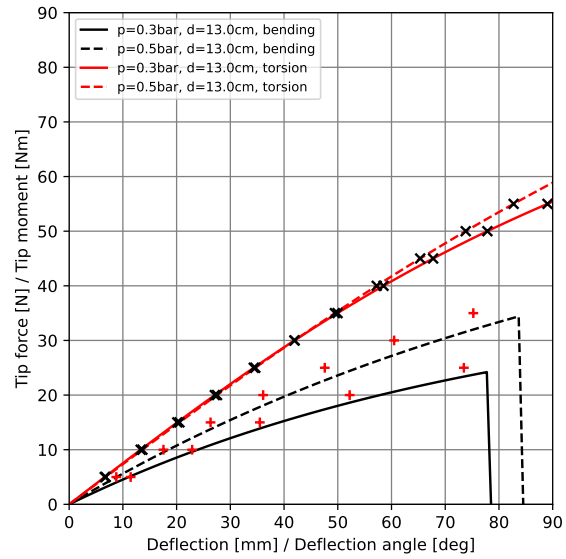
α_1 [°]	α_2 [°]	β [°]	β_2 [°]	γ_1 [°]	γ_2 [°]
20.12	20.12	24.54	24.54	26.09	26.09

4.4.3. Inflatable beam

The inflatable beam elements are compared to Breukel's fitted equations.



(a)



(b)

Figure 4.8: Comparison of 1 meter beam elements with Breukel's equations for inflatable beams, scatter points indicate results from the FEM, lines indicate breukel's equations

TODO: add non 1m beam comparisons

5

V3 Kite Model

5.1. Simplified Model

The simplified kite model is a direct port of the PSM model by Poland [34].

5.2. Complete Model

5.3. Model validation

5.4. Aero-structural coupling

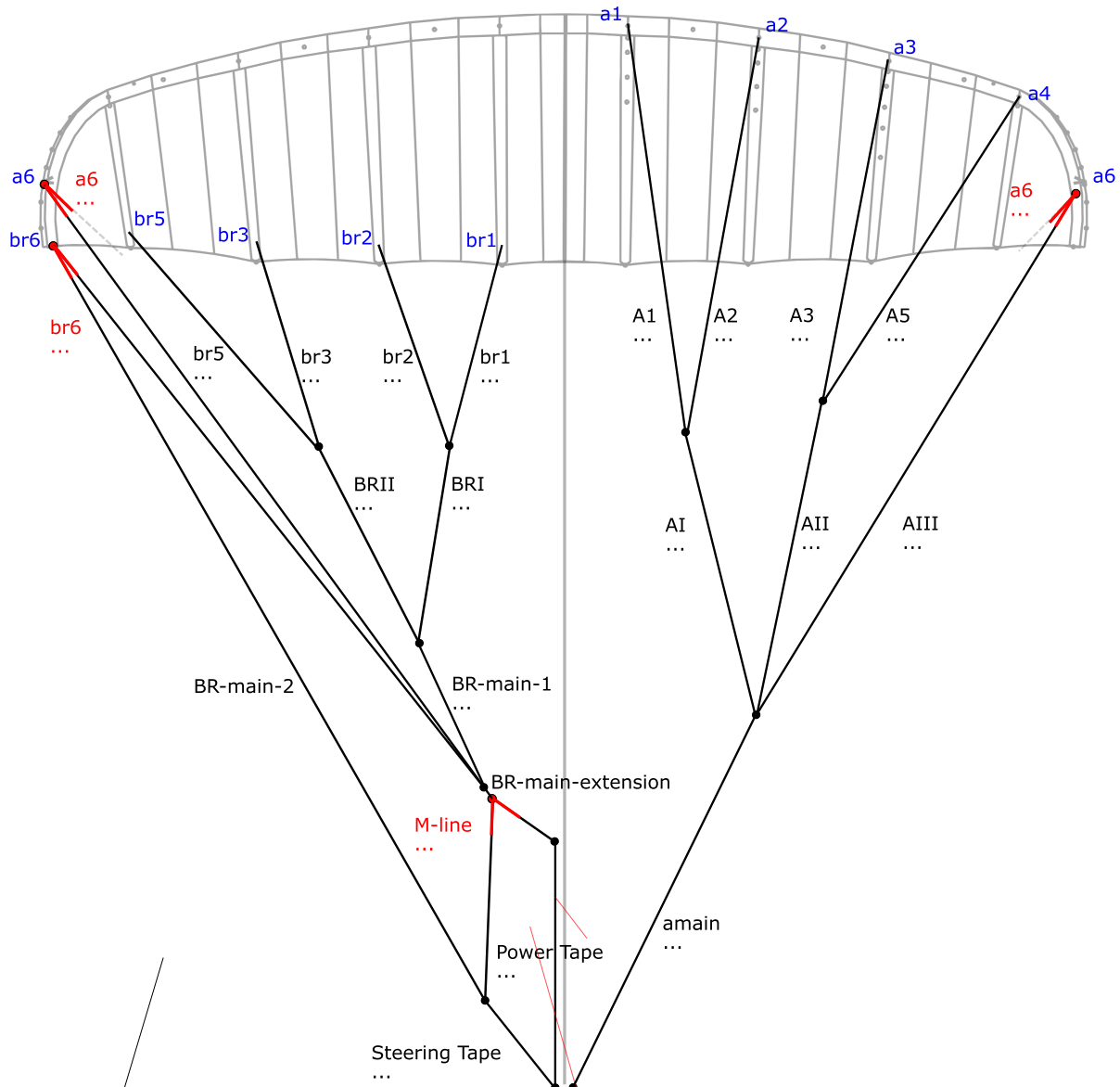


Figure 5.1: Caption (maybe put in appendix)

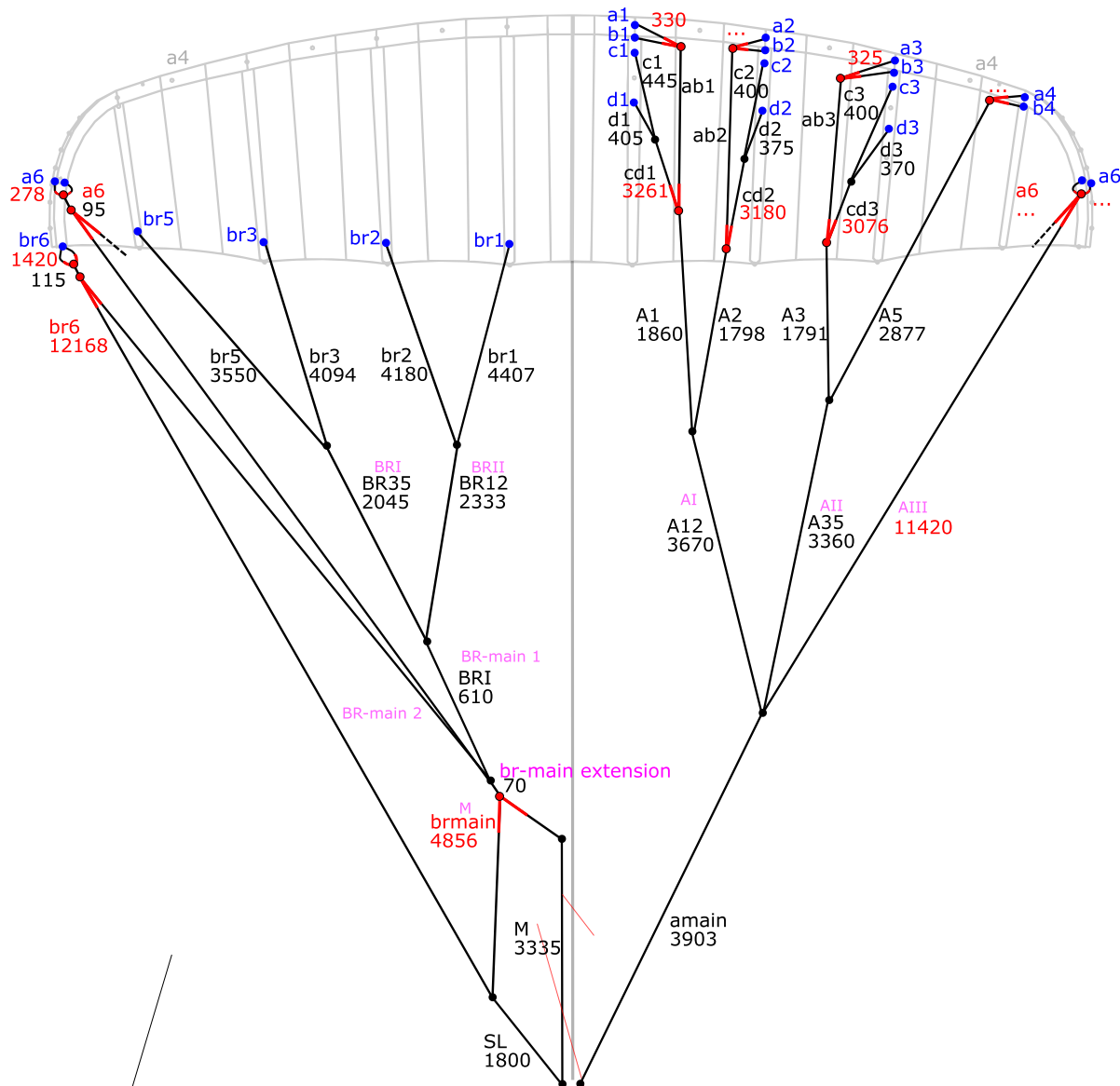


Figure 5.2: V3.25 Kite bridle configuration (maybe put in appendix)

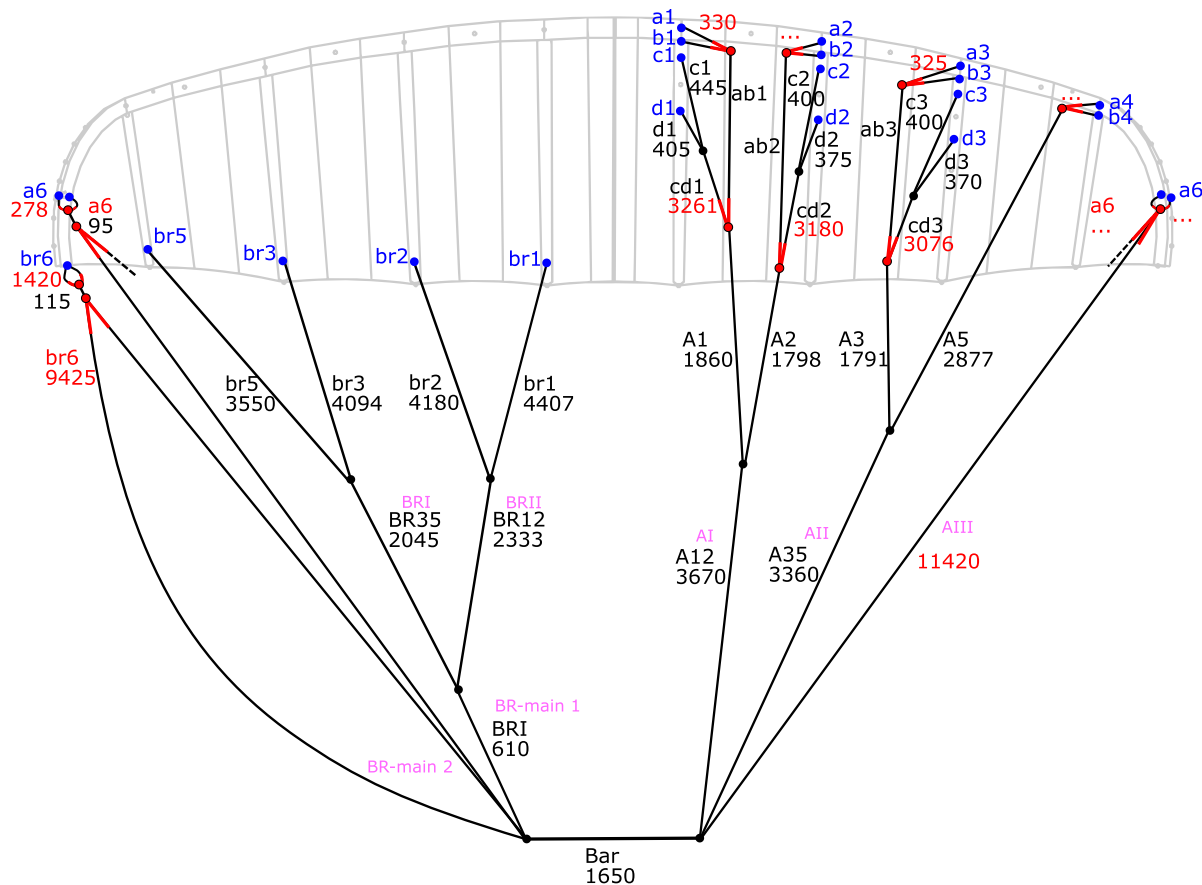


Figure 5.3: Modified V3.25 Kite bridle configuration for gravity test (maybe put in appendix)

6

Results

7

Conclusion

8

Discussion

References

- [1] M. R. Barnes. “Form finding and analysis of tension space structures by dynamic relaxation”. City University London, Oct. 1977. URL: <https://openaccess.city.ac.uk/id/eprint/11887/> (visited on 06/07/2025).
- [2] A. R. Batchelor. “Development and benchmarking of a Particle System framework for structural modeling of soft-wing kites” (2023). URL: <https://repository.tudelft.nl/record/uuid:42bd7d60-de62-4e11-ad73-5468144aaf59> (visited on 03/12/2025).
- [3] J. Berens. “Dynamic Nonlinear Aeroelastic Behaviour of Flexible Wings in an Airflow” (2015). URL: <https://repository.tudelft.nl/record/uuid:aa859e12-1087-46a5-80c6-7e63053a017a> (visited on 05/01/2025).
- [4] H. A. Bosch. “Finite Element Analysis of a Kite for Power Generation” (2012). URL: <https://repository.tudelft.nl/record/uuid:888fe64a-b101-438c-aa6f-8a0b34603f8e> (visited on 04/24/2025).
- [5] J Breukels and Wubbo Ockels. “Analysis of complex inflatable structures using a multi-body dynamics approach” (2008). URL: <https://repository.tudelft.nl/record/uuid:82a736f6-c4fa-467a-a6f1-78b88620962b> (visited on 08/27/2025).
- [6] J. Breukels. “An engineering methodology for kite design”. 2011. URL: <https://repository.tudelft.nl/record/uuid:cdece38a-1f13-47cc-b277-ed64fdda7cdf> (visited on 03/18/2025).
- [7] Saullo G. P. Castro. *General-purpose finite element solver based on Python and Cython*. Oct. 2024. DOI: 10.5281/ZENODO.6573489.
- [8] Oriol Cayon, Mac Gaunaa, and Roland Schmehl. “Fast Aero-Structural Model of a Leading-Edge Inflatable Kite” (Jan. 2023). P. 3061. DOI: 10.3390/en16073061.
- [9] Oriol Cayon, Simon Watson, and Roland Schmehl. “Kite as a Sensor: Wind and State Estimation in Tethered Flying Systems” (Jan. 2025). Pp. 1–41. DOI: 10.5194/wes-2024-182.
- [10] R. L. Comer and Samuel Levy. “Deflections of an inflated circular-cylindrical cantilever beam” (July 1963). Pp. 1652–1655. DOI: 10.2514/3.1873.
- [11] Pieter-Jan Declercq. “Analyse van het aero-elastisch gedrag van een flexibele vlieger voor windenergie” (2022). URL: <http://lib.ugent.be/catalog/rug01:003063362>.
- [12] Uwe Fechner et al. “Dynamic model of a pumping kite power system” (Nov. 2015). Pp. 705–716. DOI: 10.1016/j.renene.2015.04.028.
- [13] Carlos Felippa. “A Systematic Approach to the Element-Independent Corotational Dynamics of Finite Elements” (Jan. 2000).
- [14] Mikko Folkersma, Roland Schmehl, and Axelle Viré. “Steady-state aeroelasticity of a ram-air wing for airborne wind energy applications” (Sept. 2020). P. 032018. DOI: 10.1088/1742-6596/1618/3/032018.
- [15] Allister Furey and Inman Harvey. “Evolution of Neural Networks for Active Control of Tethered Airfoils” (2007). Pp. 746–755. DOI: 10.1007/978-3-540-74913-4_75.

- [16] N. H. Geschiere. "Dynamic modelling of a flexible kite for power generation" (2014). URL: <https://repository.tudelft.nl/record/uuid:6478003a-3c77-40ce-862e-24579dcd1eab> (visited on 04/24/2025).
- [17] F. J. J. M. M. Geuskens. "Conformable Pressurized Structures" (2012). URL: <https://repository.tudelft.nl/record/uuid:67fa0d80-98a9-4041-8d68-29a3ada4bd2a> (visited on 04/28/2025).
- [18] R. B. Haber and J. F. Abel. "Initial equilibrium solution methods for cable reinforced membranes part I—formulations" (June 1982). Pp. 263–284. DOI: 10.1016/0045-7825(82)90080-9.
- [19] J A W Poland. "Modeling aeroelastic deformation of soft wing membrane kites" (2022). DOI: 10.13140/RG.2.2.27851.92967.
- [20] M. C. Karadayi. "Particle System Modelling and Dynamic Simulation of a Tethered Rigid Wing Kite for Power Generation" (2016). URL: <https://repository.tudelft.nl/record/uuid:d6a2fcf8-7fce-4eb8-857b-209b9faac755> (visited on 03/18/2025).
- [21] E. F. van der Knaap. "A particle system approach for modelling flexible wings with inflatable support structures" (2013). URL: <https://repository.tudelft.nl/record/uuid:c77c5c6a-0bf7-47d5-b5bf-c5efac0c2d83> (visited on 03/12/2025).
- [22] B. Lansdorp, P. D. Williams, and Wubbo Ockels. "Flexibel Tethered Kite with Moveable Attachment Points Part I: Dynamics and Control" (2007). URL: <https://repository.tudelft.nl/record/uuid:e5e25332-aa49-41fc-ab6b-1ea13a0027a5> (visited on 04/29/2025).
- [23] B. Lansdorp, P. D. Williams, and Wubbo Ockels. "Flexible Tethered Kite with Moveable Attachment Points Part II: State and Wind Estimation" (2007). URL: <https://repository.tudelft.nl/record/uuid:99fcf865-f4e0-4e64-8fe7-389e283c7d8c> (visited on 04/29/2025).
- [24] Bas Lansdorp et al. "Modeling, Simulation, and Testing of Surf Kites for Power Generation". *AIAA Modeling and Simulation Technologies Conference and Exhibit*. Guidance, Navigation, and Control and Co-located Conferences. American Institute of Aeronautics and Astronautics, Aug. 2008. DOI: 10.2514/6.2008-6693.
- [25] A. Le van and C. Wielgosz. "Bending and buckling of inflatable beams: Some new theoretical results" (Aug. 2005). Pp. 1166–1187. DOI: 10.1016/j.tws.2005.03.005.
- [26] Anh Le Van and Christian Wielgosz. "Finite element formulation for inflatable beams" (Feb. 2007). Pp. 221–236. DOI: 10.1016/j.tws.2007.01.015.
- [27] Rachel Leuthold. "Multiple-Wake Vortex Lattice Method for Airborne Wind Energy Membrane-Wing Kites" (2015). URL: <https://repository.tudelft.nl/record/uuid:bad76ade-81d3-4d86-a631-c45319812445> (visited on 08/27/2025).
- [28] Yunhua Luo. "An efficient 3D Timoshenko beam element with consistant shape functions" (Oct. 2008). Pp. 95–106.
- [29] Kirk Martini. "A Particle-System Approach to Real-Time Non-Linear Analysis" (). URL: https://www.academia.edu/29793801/A_Particle_System_Approach_to_Real_Time_Non_Linear_Analysis (visited on 06/10/2025).
- [30] Thouraya Nouri-Baranger. "Computational methods for tension-loaded structures" (June 2004). Pp. 143–186. DOI: 10.1007/BF02905937.
- [31] Johannes Oehler and Roland Schmehl. "Aerodynamic characterization of a soft kite by in situ flow measurement" (Jan. 2019). Pp. 1–21. DOI: 10.5194/wes-4-1-2019.

- [32] Jelle Poland, Tom Mooijman, and Corentin Tan. *SurfplanAdapter*. 2025. URL: <https://github.com/jellepoland/SurfplanAdapter>.
- [33] Jelle Poland and Roland Schmehl. *TUDELFT_V3_KITE*. Mar. 2025. URL: https://awegroup.github.io/TUDELFT_V3_KITE/.
- [34] Jelle A. W. Poland and Roland Schmehl. “Modelling Aero-Structural Deformation of Flexible Membrane Kites” (Jan. 2023). P. 5264. DOI: 10.3390/en16145264.
- [35] Jelle Agatho Wilhelm Poland and Roland Schmehl. “A virtual wind tunnel for deforming airborne wind energy kites” (June 2024). P. 072001. DOI: 10.1088/1742-6596/2767/7/072001.
- [36] Saman Sabzehzar et al. “Proposing a practical equivalent Timoshenko beam for analysis of truss structures” (May 2024). P. 106401. DOI: 10.1016/j.istruc.2024.106401.
- [37] J. F. J. E. M. Schwoll. “Finite Element Analysis of Inflatable Structures Using Uniform Pressure” (2012). URL: <https://repository.tudelft.nl/record/uuid:f92da57f-55df-4109-9f8a-8c7c2b220c6a> (visited on 03/18/2025).
- [38] Alain de Solminihac et al. “Kite as a Beam: A Fast Method to get the Flying Shape”. *Airborne Wind Energy*. Springer, Singapore, 2018, pp. 79–97. DOI: 10.1007/978-981-10-1947-0_4.
- [39] Lip H. Teh and Murray J. Clarke. “Co-rotational and Lagrangian formulations for elastic three-dimensional beam finite elements” (Nov. 1998). Pp. 123–144. DOI: 10.1016/S0143-974X(98)00200-4.
- [40] P. Thedens. *A membrane finite element solver based on kinetic dynamic relaxation*. June 2022. URL: <https://github.com/pthedens/mem4py> (visited on 03/24/2025).
- [41] P. Thedens. “An integrated aero-structural model for ram-air kite simulations: with application to airborne wind energy”. Delft University of Technology, 2022. DOI: 10.4233/UUID:16E90401-62FC-4BC3-BF04-7A8C7BB0E2EE.
- [42] Jelte van Til et al. “Dynamic Model of a C-shaped Bridled Kite Using a few Rigid Plates”. *Airborne Wind Energy*. Springer, Singapore, 2018, pp. 99–115. DOI: 10.1007/978-981-10-1947-0_5.
- [43] D. Veenendaal and P. Block. “An overview and comparison of structural form finding methods for general networks” (Dec. 2012). Pp. 3741–3753. DOI: 10.1016/j.ijsolstr.2012.08.008.
- [44] Sebastiaan Leopold Veldman. “Design and analysis methodologies for inflated beams”. Netherlands: Technische Universiteit Delft (The Netherlands), 2005. URL: <https://www.proquest.com/docview/305372243/abstract?sourceType=Dissertations%20&%20Theses> (visited on 04/28/2025).
- [45] Junsong Wang et al. “An active-bending sheltered pathway based on bamboo strips for indoor temporary applications: Design and construction” (May 2024). P. 117863. DOI: 10.1016/j.engstruct.2024.117863.
- [46] Christian Wielgosz, Jean-Christophe Thomas, and Pascal Casari. “Strength of Inflatable Fabric Beams at High Pressure” (Apr. 2002). DOI: 10.2514/6.2002-1292.
- [47] Qiu Zhang et al. “Development of an active bending temporary corridor based on bamboo strips: preliminary results”. Aug. 2021.